

PAPER • OPEN ACCESS

## Shape control and whole-life energy assessment of an ‘infinitely stiff’ prototype adaptive structure

To cite this article: Gennaro Senatore *et al* 2018 *Smart Mater. Struct.* **27** 015022

View the [article online](#) for updates and enhancements.

### Related content

- [The European Spallation Source Design](#)  
Roland Garoby, H Danared, I Alonso et al.
- [A study on the design and behavior of smart antenna](#)  
U Saravanan, Srinivasan M Sivakumar and V Kalyanaraman
- [Co-rotational thermo-mechanically coupled multi-field framework and finite element for the large displacement analysis of multi-layered shape memory alloy beam-like structures](#)  
Alexandros G Solomou, Theodoros T Machairas, Anargyros A Karakalas et al.

# Shape control and whole-life energy assessment of an ‘infinitely stiff’ prototype adaptive structure

Gennaro Senatore<sup>1</sup> , Philippe Duffour<sup>2</sup> , Pete Winslow<sup>3</sup> and Chris Wise<sup>3</sup>

<sup>1</sup>Swiss Federal Institute of Technology (EPFL), School of Architecture, Civil and Environmental Engineering (ENAC), Applied Computing and Mechanics Laboratory (IMAC), Station 18, CH-1015 Lausanne, Switzerland

<sup>2</sup>University College London, Gower Street, WC1E 6BT, London, United Kingdom

<sup>3</sup>Expedition Engineering, 4 Maguire St, SE1 2NQ, London, United Kingdom

E-mail: [gennaro.senatore@epfl.ch](mailto:gennaro.senatore@epfl.ch)

Received 20 April 2017, revised 20 August 2017

Accepted for publication 14 September 2017

Published 18 December 2017



CrossMark

## Abstract

A previously developed design methodology produces optimum adaptive structures that minimise the whole-life energy which is made of an embodied part in the material and an operational part for structural adaptation. Planar and complex spatial reticular structures designed with this method and simulations showed that the adaptive solution achieves savings as high as 70% in the whole-life energy compared to optimised passive solutions. This paper describes a large-scale prototype adaptive structure built to validate the numerical findings and investigate the practicality of the design method. Experimental results show that (1) shape control can be used to achieve ‘infinite stiffness’ (i.e. to reduce displacements completely) in real-time without predetermined knowledge regarding position, direction and magnitude (within limits) of the external load; (2) the whole-life energy of the structure is in good agreement with that predicted by numerical simulations. This result confirms the proposed design method is reliable and that adaptive structures can achieve substantive total energy savings compared to passive structures.

Keywords: prototype adaptive structure, shape control, load-path optimisation, whole-life energy, structural optimisation

(Some figures may appear in colour only in the online journal)

## Glossary

$\alpha$	cross section areas ( $n \times 1$ )	$\beta$	total strain ( $n \times 1$ )
$A^{EQ}$	equilibrium constraints [ $m \times (n + n^R)$ ]	$\beta^e$	elastic strain ( $n \times 1$ )
$A^{ULS}$	ULS constraints [ $2 \cdot n \times (n + n^R)$ ]	$\beta^0$	eigenstrain ( $n \times 1$ )
$A^{ULSB}$	nonlinear ULS constraints [ $n \times (n + n^R)$ ]	$C$	geometric compatibility ( $r \times n$ )
$B^{RED}$	reduced (excludes constrained degrees of freedom) equilibrium matrix [ $(m - n^R) \times n$ ]	CDOF	controlled degree of freedom
		$\Delta L$	actuator length changes ( $n \times 1$ )
		$\Delta L^{RED}$	reduced actuator length changes ( $n^{ACTs} \times 1$ )
		DOF	degree of freedom
		$\Delta F$	load-path redirection ( $F - F^{COMP}$ ) ( $n \times 1$ )
		$\Delta u$	displacement correction ( $u^{SLS} - u^{COMP}$ ) ( $m \times 1$ )



Original content from this work may be used under the terms of the [Creative Commons Attribution 3.0 licence](https://creativecommons.org/licenses/by/3.0/). Any further distribution of this work must maintain attribution to the author(s) and the title of the work, journal citation and DOI.

$\eta$	actuator mechanical efficiency
$\mathbf{F}$	optimal (non-compatible) forces ( $n \times 1$ )
$\mathbf{F}^{\text{EXT}}$	extended (includes reactions) optimal forces [ $(n + n^R) \times 1$ ]
$\mathbf{F}^{\text{COMP}}$	compatible forces ( $n \times 1$ )
$\mathbf{G}$	flexibility matrix ( $n \times n$ )
IFM	integrated force method
$\mathbf{J}$	IFM deformation coefficient matrix [ $(m - n^R) \times n$ ]
$\mathbf{L}$	structural element lengths ( $n \times 1$ )
$m$	number of degrees of freedom
MUT	material utilisation factor
$n$	number of structural elements
$n^{\text{ACTs}}$	number of actuators
$n^R$	number of constrained degrees of freedom
$n^P$	number of load cases
$n^{\text{CDOFs}}$	number of controlled degrees of freedom
$\mathbf{P}$	external load ( $m \times 1$ )
$\mathbf{P}^{\text{RED}}$	reduced external load [ $(m - n^R) \times 1$ ]
$\mathbf{P}^{\text{EIG}}$	eigenstrain load ( $r \times 1$ )
$\mathbf{P}^*$	IFM external load ( $n \times 1$ )
$r$	degree of static indeterminacy
$\mathbf{S}$	IFM governing matrix ( $n \times n$ )
$\mathbf{S}^F$	actuation force sensitivity matrix ( $n \times n$ )
$\mathbf{S}^{F \text{RED}}$	reduced actuation force sensitivity matrix ( $n \times n^{\text{ACTs}}$ )
$\mathbf{S}^u$	actuation displacement sensitivity matrix ( $m \times n$ )
$\mathbf{S}^{u \text{CDOFs}}$	reduced actuation displacement sensitivity matrix ( $n^{\text{CDOFs}} \times n$ )
$\mathbf{S}^{u \text{RED}}$	reduced actuation displacement sensitivity matrix ( $n^{\text{CDOFs}} \times n^{\text{ACTs}}$ )
SLS	serviceability limit state
S/D	span-to-depth ratio
$\mathbf{u}^{\text{COMP}}$	compatible nodal displacements ( $m \times 1$ )
$\mathbf{u}^{\text{SLS}}$	required nodal displacements ( $m \times 1$ )
ULS	ultimate limit state
$\mathbf{x}^{\text{ACTs}}$	actuator stroke position ( $n \times 1$ )

## 1. Introduction

Adaptive structures are defined here as structures capable of counteracting actively the effect of external loads via controlled shape changes and redirection of the internal load paths. These structures are integrated with sensors (e.g. strain, cameras), actuators and control intelligence.

In civil engineering, active control has focussed mostly on the control of vibrations for building or bridges to improve safety and serviceability during exceptionally high loads (i.e. strong winds, earthquakes) [1, 2]. Active brace systems have been tested using hydraulic actuators fitted as cross-bracing elements of the structure, controlling directly its response using actively controlled forces [3–5]. Displacement control in cable stayed bridges can be obtained via control forces provided by the stay cables working as active tendons [6, 7]. Active cable-tendons can also be used to change the amount of pre-stress in reinforced concrete beams and in steel trusses to limit displacements under loading [8]. The integration of actuators has been shown to be an effective way to suppress vibrations in high stiffness/weight ratio truss structures [9].

Active structural control has also been used in applications for shape control. Some all-weather stadia use deployable systems for expandable/retractable roofs e.g. the Singapore National Stadium [10] and the Wimbledon Centre Court [11]. Active tensegrity structures whose stability depends on self-stress, have been used as deployable systems in aerospace [12] and civil engineering applications [13, 14]. Active compliant structures, which can be thought of as structures working as monolithic mechanisms [15, 16], have been studied for deployment of antenna reflectors and shape control of aircraft wings to improve on manoeuvrability [17].

Actuation has been used to modify the membrane stress state in thin plates and shells to help them cope with unusual loading events [18] or when the load carrying capacity is reduced because of Residual stresses formed after welding, machining or formworks removal [19]. In the event of such disturbances, actuation in the form of induced strain distributions or induced displacements of the supports (actively controlled bearings) can be used to homogenise the stress field and in so doing minimising the maximum stress governing the design [20].

Adaptive structures have a good potential for mitigating strong hazard events and control of displacements/vibrations in deflection-sensitive structures [21]. Because of uncertainties regarding the long-term reliability of sensor and actuator technologies combined with building long service lives and load long return periods, the recent trend has been to develop active structural control to help satisfy serviceability requirements rather than contribute to strength/safety improvement [22].

Most design strategies for adaptive structures aim to minimise a combination of control effort and material mass of the structure. Often the structure and the actuation system are designed as separate systems—the location of sensors/actuators being decided *a priori* [21, 23, 24]. However, a well-chosen actuator layout is critical to minimising control effort and improving accuracy. The majority of existing methods that address the actuator-placement problem rely on meta-heuristics [25, 26] which give little insight into the mechanics of active force/displacement control. In addition, although the potential of using adaptation to save material mass has been investigated by a few [27–29], whether the energy saved by using less material makes up for the energy



**Figure 1.** Adaptive truss prototype, University College London Structures Laboratory.

consumed through control and actuation is a question that has so far received little attention.

Senatore *et al* [30, 31] proposed a novel adaptive structure design method whereby the active system is only used when necessary to ensure the whole life energy of the structure is kept to a minimum. Whole life energy is here understood as the sum of the embodied energy in the material and the operational energy used by the active control system. Using this methodology, they showed using simulation work on a range of planar and complex spatial reticular structures that energy savings as high as 70% can be achieved when compared to identical passive structures designed using state art optimisation methods. These studies confirm that adaptive structures achieve superior performance when the design is stiffness-governed. For slender structures the adaptive solution outperforms the passive one in energy terms not only for extreme but also for ordinary loading events and it can even compete in monetary terms.

A purpose-built large scale prototype structure (here named ‘adaptive truss’) was built in University College London Structures Laboratory for experimental testing. The prototype, shown in figure 1, is a cantilevered platform designed to withstand a person walking along its length. It was designed using the methodology proposed by Senatore *et al* [30]. There were three main motivations for doing this: (1) to demonstrate the potential of the design methodology on a realistic example; (2) to investigate the practicality and feasibility of the design process when applied to a real structure; (3) to validate numerical predictions against experimental data.

This paper starts with a summary of the design methodology used to design the prototype. This is followed by a detailed description of the prototype structure and its control system including the implementation of control software. The

focus later moves to the description of the experiments carried out to assess control performance and power consumption during shape control.

## 2. Background on adaptive design methodology

A novel design methodology for adaptive structures was presented in Senatore *et al* [30, 31]. This method is based on improving structural performance by reducing the energy embodied in the material at the cost of a small increase in operational energy necessary for structural adaptation. The method is briefly summarised here. The reader is referred to [30] for a more comprehensive presentation. The method comprises two nested optimisation processes as shown by the flowchart in figure 2.

The outer optimisation searches the structure with minimum whole life energy by varying the Material Utilisation Factor (MUT). This MUT is a ratio of the strength capacity over demand but it is defined for the structure as a whole and can be effectively thought of as a scaling factor on the allowable stresses. Figure 3 shows notionally the variation of the total energy as the MUT varies. By varying the material utilisation factor one can move from least-weight structures with small embodied but large operational energy, to stiffer structures with large embodied and smaller operational energy consumption. The active-passive system corresponding to the minimum of the sum of embodied and operational energy is the configuration of the optimum sought.

The inner optimisation itself consists of two main routines. The first routine finds the optimum load path and corresponding material distribution ignoring compatibility and serviceability limit states, thus obtaining a lower bound in

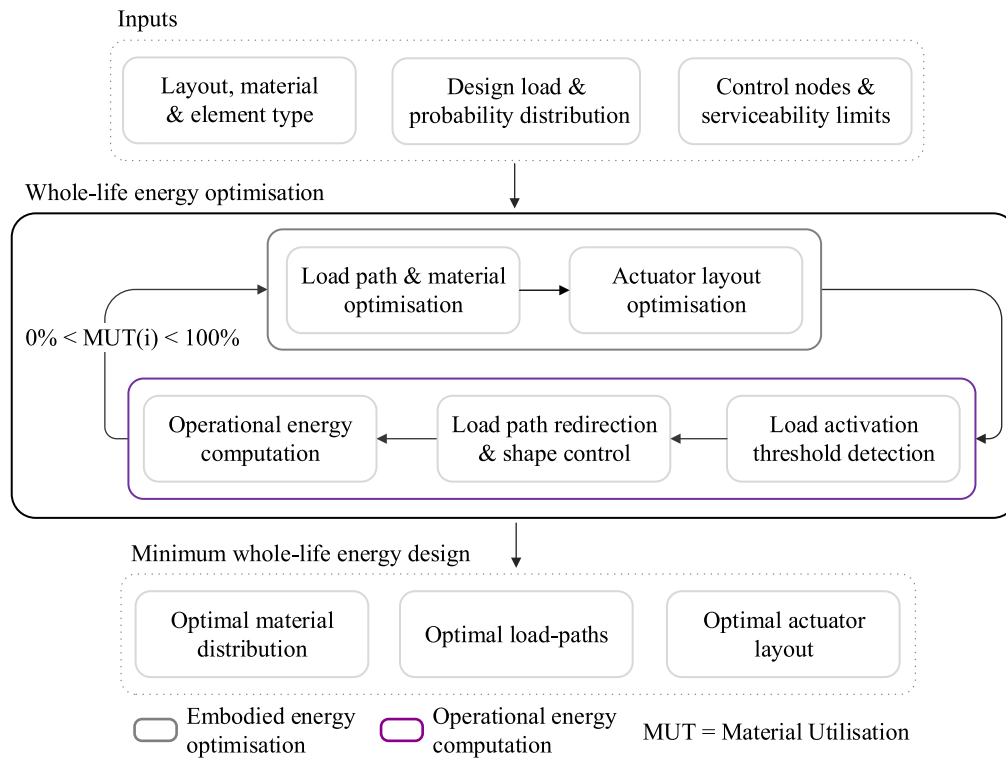


Figure 2. Design methodology flowchart.

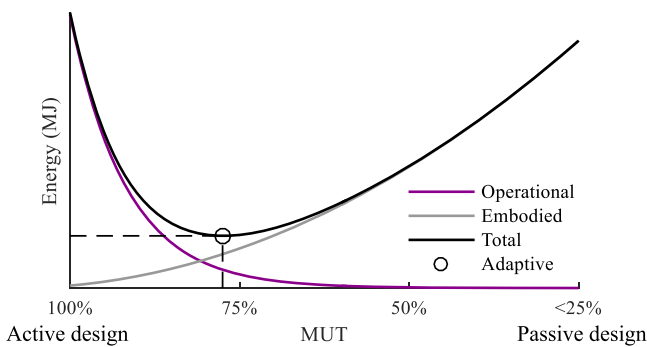


Figure 3. Embodied, operational and total energy as a function of the material utilisation factor (MUT).

terms of material mass and thus embodied energy. When external loads are applied to the structure, the compatible forces will in general be different from the optimal forces and the resulting displacements might be beyond serviceability limits. For this reason, the second routine finds the optimal number and position of the actuators which are thought of as integrated into the structure by replacing some of its members. Once the actuator layout in known, a control strategy is determined. If a change in the loads causes a state of stress that violates an ultimate limit state (ULS) or a serviceability limits state, the load path is redirected and displacements are controlled by the active system. The actuator length changes manipulate actively the flow of internal forces and compensate for displacements enforcing compatibility by changing

the shape of the structure. In this way, the stresses are homogenised and the displacements are reduced within required serviceability limits. Passive resistance through material and form is replaced by a small amount of operational energy.

The proposed design process can be particularly beneficial when the design is governed by large loading events that have a small probability of occurrence (storms, earthquakes, unusual crowds but also moving loads such as trains). For simplicity, these loads will be considered as live loads here because they are not permanent. To illustrate this, figure 4(a) shows a notional cumulative frequency of occurrence plot for a generic stochastic load. The dotted line represents the activation threshold which demarcates two zones: on the left-hand side are the more probable low levels of load the structure will be able to withstand passively without actuation. On the right are the rarer loads with higher magnitude which the structure will only be able to resist using both passive and active load-bearing capacity. The two zones of the load range can also be visualised in figure 4(b) which shows the hours of occurrence of the live load whose distribution is divided in discrete steps from zero to the design load.

The introduction of the load activation threshold shows how passive and active design can be combined to reach a higher level of efficiency. The hybrid passive-active structural system is designed so that in normal loading conditions it can take the load using only its passive capacity with the actuators locked in position. The actuators are only activated when the

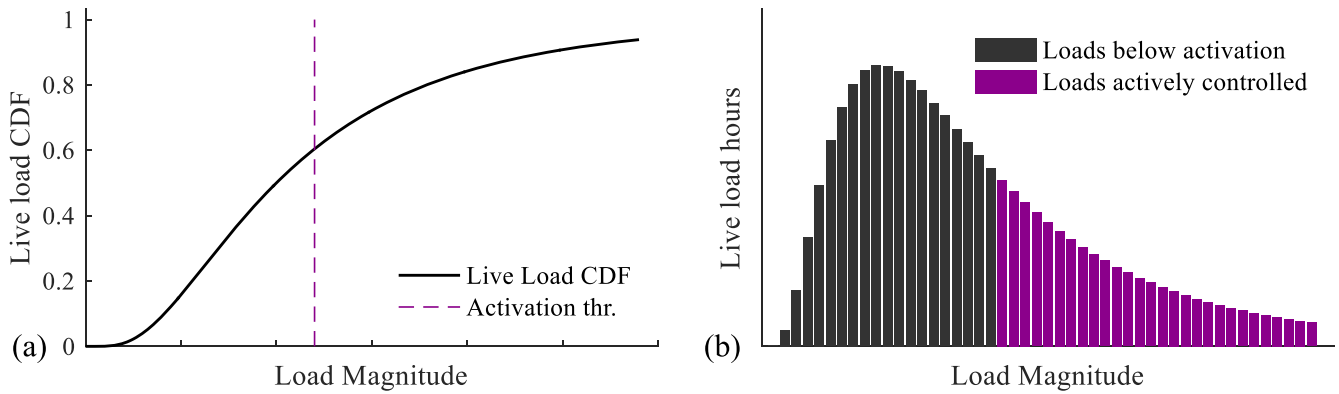


Figure 4. (a) Live load cumulative distribution; (b) live load hours.

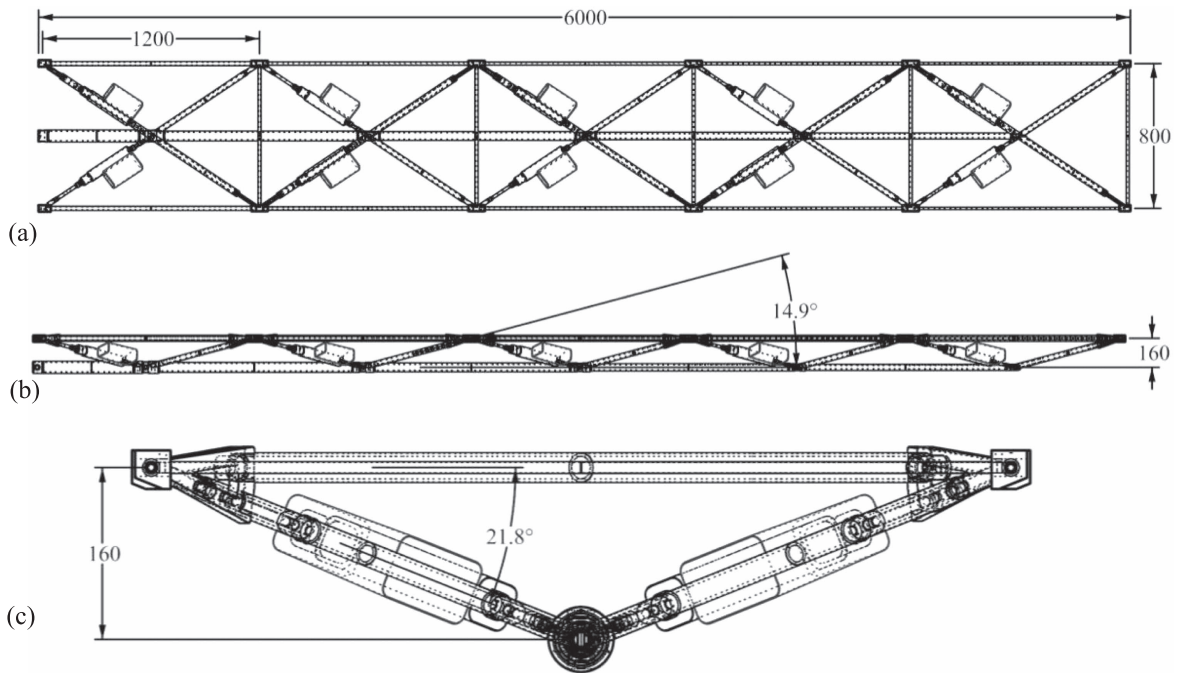


Figure 5. Adaptive truss dimensions (a) plan view, (b) elevation, (c) side view.

loads reach the activation threshold and therefore the operational energy is only used when necessary.

### 3. Description of the adaptive truss prototype

#### 3.1. The underlying reticular structure

The adaptive truss prototype is a 6000 mm long, 800 mm wide cantilevered platform supported by pins 1 m above ground. The horizontal supporting structural systems is a very slender—160 mm deep, space frame which has a span-to-depth ratio of 37.5:1. The truss consists of 5 bays, 1.2 m long each. Figure 5 shows the overall dimensions of the truss in plan, elevation and side views. The active elements, visible in figure 1 and represented to scale in figure 5, are electro-mechanical actuators fitted within some of the diagonal bracing. The control system sits at the back of the vertical supporting bracket as shown in figure 1.

The truss is designed to support its own weight which consists of 52 kg for the steel structure, 50 kg for the actuators (5 kg each) and 70 kg for the acrylic deck panels and housing (approximately  $17 \text{ kg m}^{-2}$ ). In addition to its self-weight, the structure can take a live load of 100 kg at the tip of the cantilever. The live load is thought of as a person walking along the deck. The live load is modelled as three load cases (figure 6) representing the worst scenarios when the person stands at the free end with their weight distributed equally between the two end nodes (black arrows) or when their entire weight is concentrated on either one of them (blue/red arrow). Note that the truss is not quite symmetrical so these two unbalanced load cases are different. Some of the dynamic effects caused by walking are considered using an additional load factor to ensure safety but the primary concern in this paper is the quasi-static behaviour of the structure. Displacement control tests were always carried out at moderate ‘walking’ speed to make sure dynamic amplification would

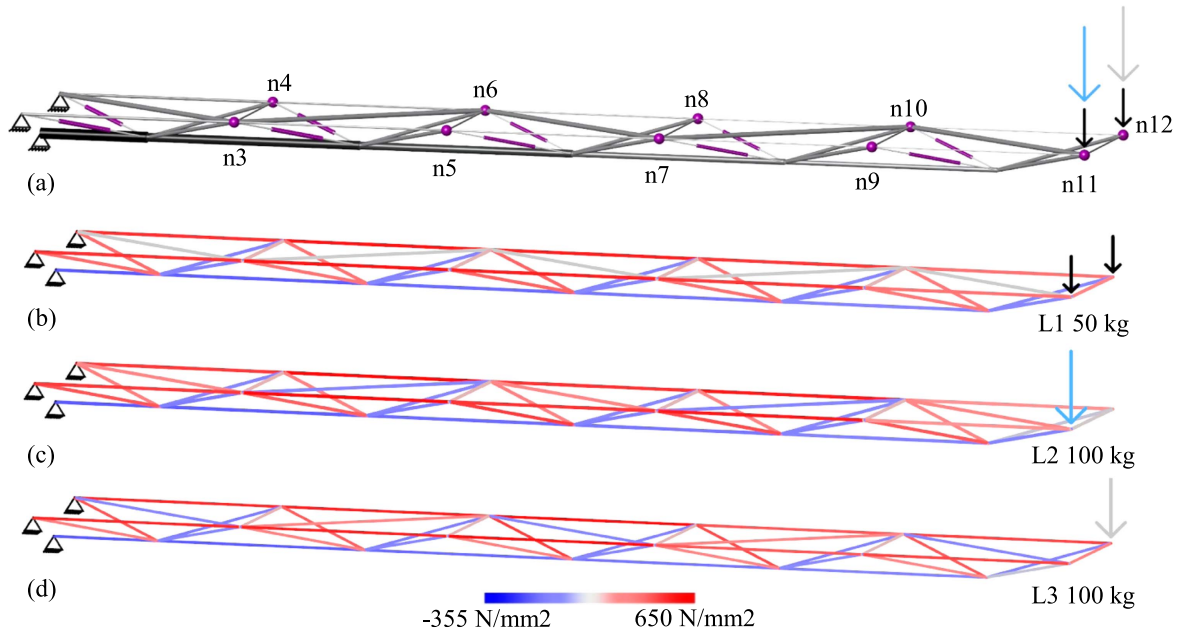


**Figure 6.** (a) Truss elements, loads, controlled nodes indicated by spheres; (b)–(d) element stress.

**Table 1.** Adaptive truss prototype load combination cases.

	Permanent load (PL)	Dynamic	Live load	Characteristic load
LC1	1.35 Deck + self-weight	1.5	1.4 L1	95th
LC2	1.35 Deck + self-weight	1.5	1.4 L2	95th
LC3	1.35 Deck + self-weight	1.5	1.4 L3	95th

**Table 2.** Elements numbering, cross section dimensions and material.

	Element number	Steel grade	Outer diameter (mm)	Wall thickness (mm)
Top chord rods (longitudinal)	1–2	EN24T	16	n/a
	3–5	EN24T	12	n/a
	6–8	EN24T	10	n/a
	9–11	EN24T	8	n/a
	12–14	EN24T	6	n/a
Top chord rods (transversal)	4–7–10–13–15	EN24T	10	n/a
Top chord tubes bracers	16–17–18–19–20	S355	26.67	2.87
Diagonal rods (actuators)	26–27–30–31	EN24T	10	n/a
	34–35–38–39–42–43	EN24T	8	n/a
Bottom chord tubes	21	S355	60.33	3.91
	22	S355	48.26	3.68
	23	S355	42.16	3.56
	24	S355	33.4	3.38
	25	S355	26.67	3.91
Diagonal tubes	28–29–32–33–36–37–40–41–44–45	S355	21.34	2.77

not occur. Table 1 gives a summary of the load cases and their combination.

The members of the structure are sized to meet the worst expected ‘demand’ from all load cases to be fully compliant to Eurocode 3 [32] in terms of ULS but ignoring deflection requirements. This is because instead of using more material to meet serviceability requirements, strategically placed active

elements (i.e. actuators) keep deflections within limits by changing the shape of the structure when loading exceed the load activation threshold (see section 4.1.3).

There are 45 elements of which 20 are solid high strength steel round bars (EN24T) and 25 are structural steel tubes (S355). The size of the element cross-section diameters ranges from 16 to only 6 mm for of the tie-bars and 60.33 to 21.34 mm

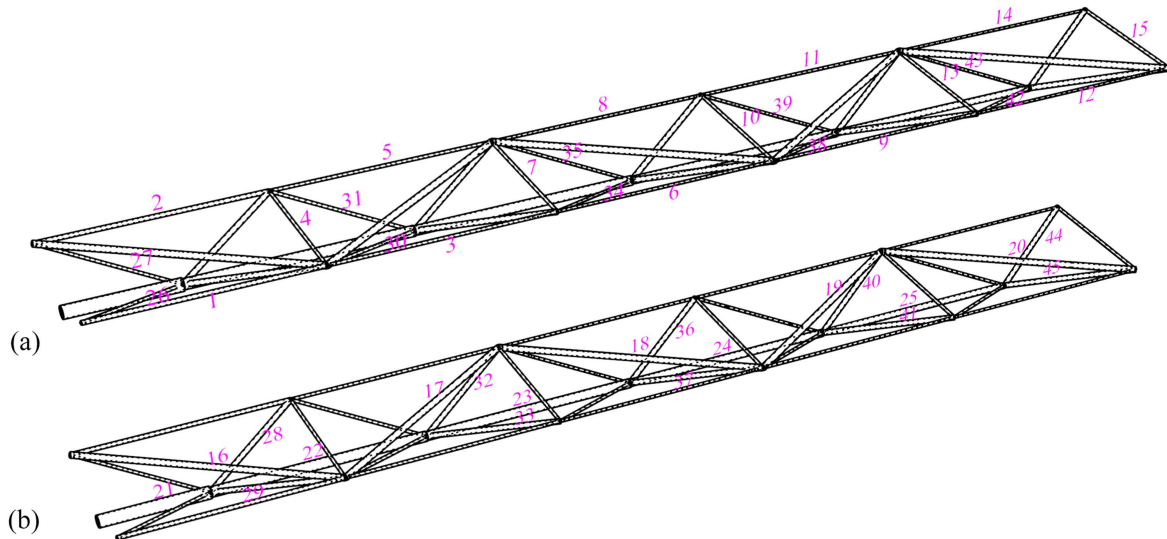


**Figure 7.** Perspective view of the truss with labels for (a) solid bars and (b) tubes.

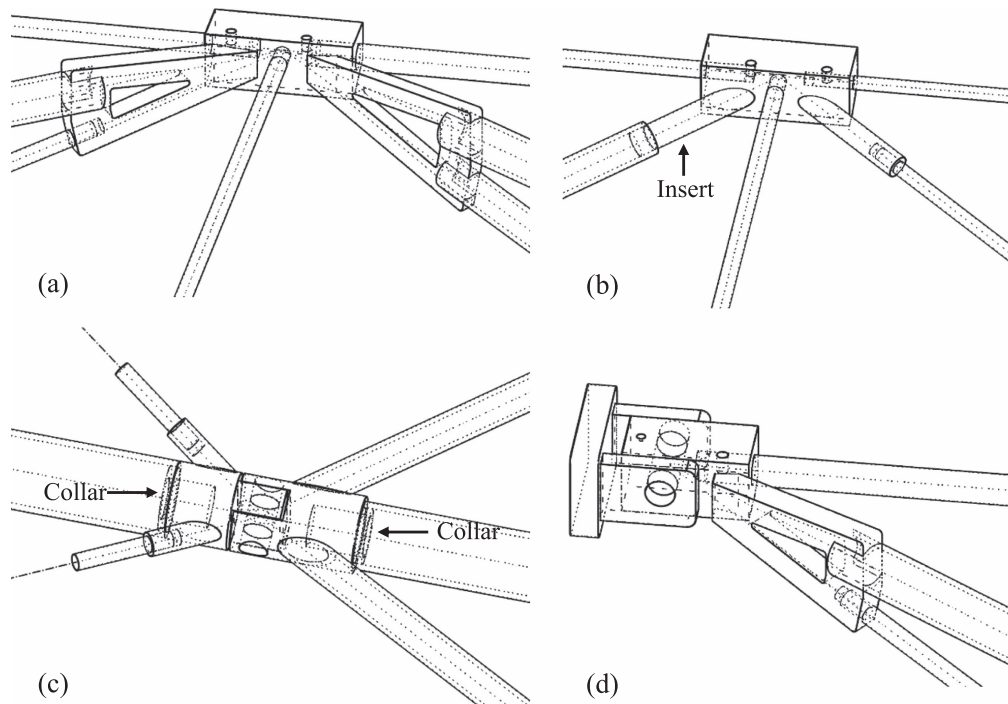


**Figure 8.** Perspective view of joint configurations, (a) top-chord 7-elements, (b) top-chord 5-elements; (c) bottom chord 6-elements; (d) pin joint connected to bracket.

for the tubes (average wall thickness is 3 mm). The round bars are utilised to carry tension along the top chords and as part of the actuator fitting system. The main reason for using high strength steel for the tension members is to reduce further the dimension of their cross sections due to space constraints at the nodes where up to 7 elements converge into one point (section 3.2). The tubes are utilised to take compressive forces along the bottom chord and the front diagonal bracers for each bay. In addition, tubes are also placed as the diagonal bracers of

the top chords to counteract loads causing overall torsion of the truss (c and d in figure 6). Table 2 details section dimensions and materials and figure 7 gives the element numbering.

### 3.2. Joints

Optimal material distribution and the remarkable slenderness of the structure posed challenges for the design and manufacture of the joints. Although each joint is different because



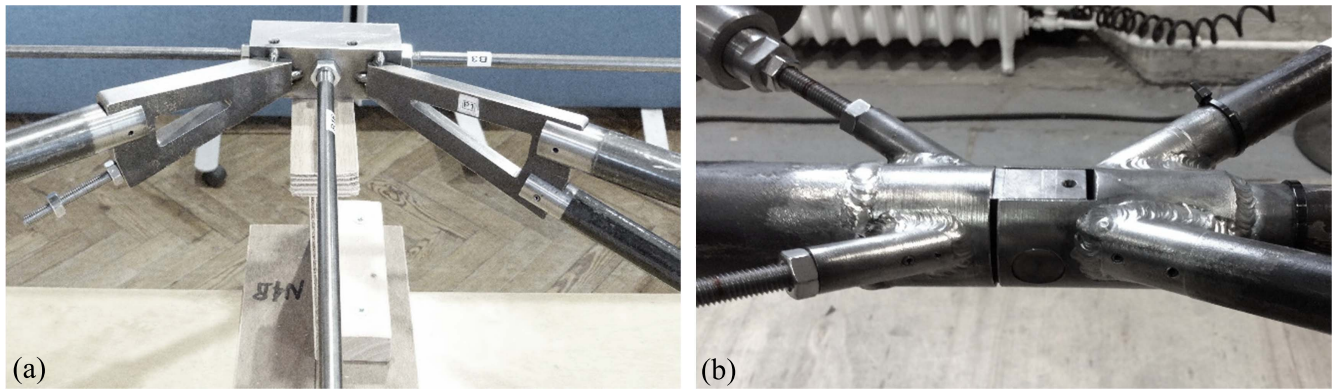


Figure 9. (a) Top cord node; (b) bottom cord node.

the elements have different section sizes, there are four main configurations as shown in figure 8: (a) top chord joint connecting 7 elements; (b) top chord joint connecting 5 elements; (c) bottom chord joint connecting 6 elements; (d) end joints.

Each joint was designed so that the elements it connects converge to a single point. All joints consist of a central piece made from a solid structural steel bar (S355) machined into a brick shaped node or a cylindrical shaped node for top and bottom chords respectively. Triangle shaped plates, cylindrical couplers, inserts and collars are used to connect the nodes with the elements. The inserts and collars for node types (b) and (c) ensure a stable and accurately controlled position of the elements with respect to the node.

To minimise the weight of the joints, material was removed by chamfering the brick shaped nodes, by making blind holes inside the cylindrical shaped nodes and through holes in the triangle shaped plates. All bar members are connected using left and right threads to allow the node positions to be fine-tuned prior to welding during assembly and to allow the actuators to be taken out for maintenance. The joints at the supports (d) have pins to avoid moment transfer between the truss and the frame used as a fixed end. Pins are also inserted into the joints at mid-length of the truss to allow it to be spliced into two 3 m parts for ease of transportation. Figure 9 shows photographs of joint type (a) and (c).

The joints were designed following Eurocode 3 [32]. Combined shear and bending resistance were taken into account. Due to the complexity of their geometry, the joints were experimentally tested under combined loads.

Construction tolerances on the position of two consecutive nodes was set within  $\pm 2$  mm. This value resulted from modelling misalignment between the nodes to check that members in compression do not reach capacity (i.e. critical loads) due to position inaccuracy. As an additional preventive measure, a single articulated pinned joint was added at the bottom chord nodes (c) to minimise the transfer of bending moment across the bottom chord whose primary function is to carry high compressive forces (up to 132 kN). A frame with adjustable supports was built to control precisely the position of the nodes during construction and welding. Once aligned the nodes were welded using tungsten inert gas.

### 3.3. Deck

The deck/façade of the structure consists of a series of aluminium angle profiles which house transparent acrylic panels as shown in figure 10(a). Clear acrylic was chosen to allow the actuator length changes to be seen during control. The aluminium angles also provide housing to power and signal cables which are bundled and clipped to their bottom face as shown in figure 10(b).

To ensure the aluminium angle profiles do not contribute to the stiffness of the truss, one of their ends is free to slide using the arrangement shown in figure 11. A countersunk screw (shown in magenta) is placed into the node going through the slot in the aluminium angle and the neoprene pad that sits between the node and the angle. The head of the screw sits flush on the slot to prevent vertical movement of the angle. The other end of the angle profile is instead fixed to the node. This way each bay of the deck can move independently from the adjacent ones.

## 4. Control system

The control system architecture is designed with the primary aim to achieve identification of the response to loading in terms of internal forces and displacements for the structure to be able to control itself without user intervention nor predetermined knowledge of the external load (position, direction or magnitude). The control hardware consists of ten linear actuators, a control driver board for each pair of actuators, 45 strain gauge based sensors, two amplifiers for signal conditioning and a main controller for acquisition and processing. Figure 12 shows conceptual schematics for the control system architecture.

The deformation of each element, monitored using strain gauge-based sensors of type full-bridge, together with the actuator stroke position feedback are fed into the main controller. These control inputs are processed to reconstruct the node spatial positions to assess whether their displacements exceed required serviceability limits. In this case, the actuators vary their stroke length to change the shape of the structure so that displacements of the controlled nodes are reduce within required limits. Input commands to the

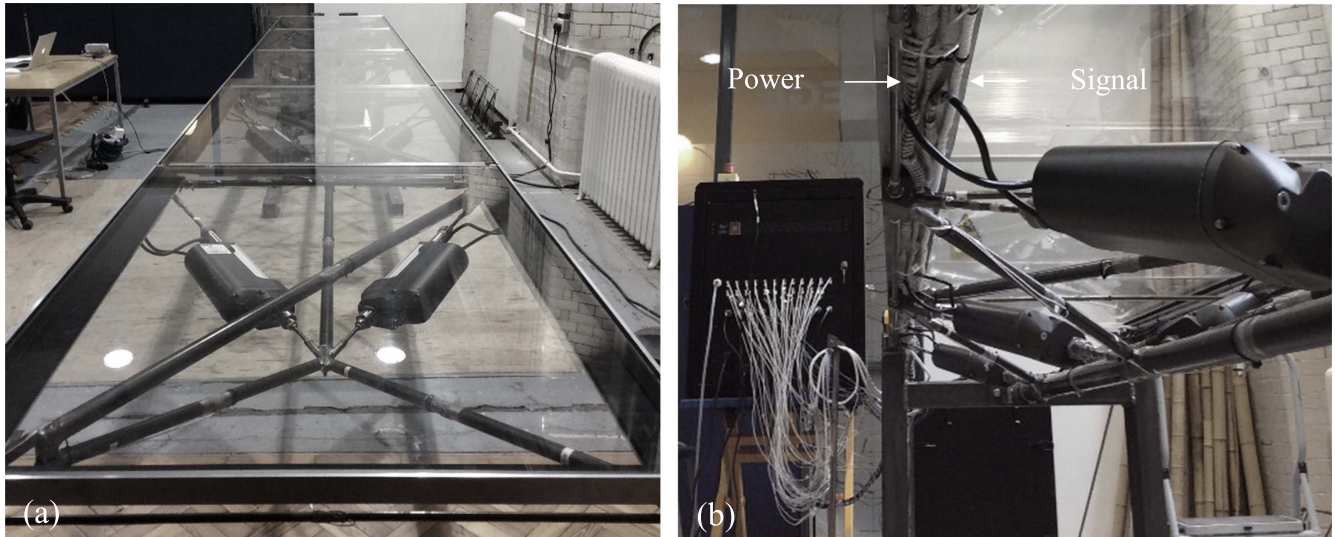


**Figure 10.** (a) Acrylic panels; (b) signal and power cables bundles clipped underneath the aluminium angles.

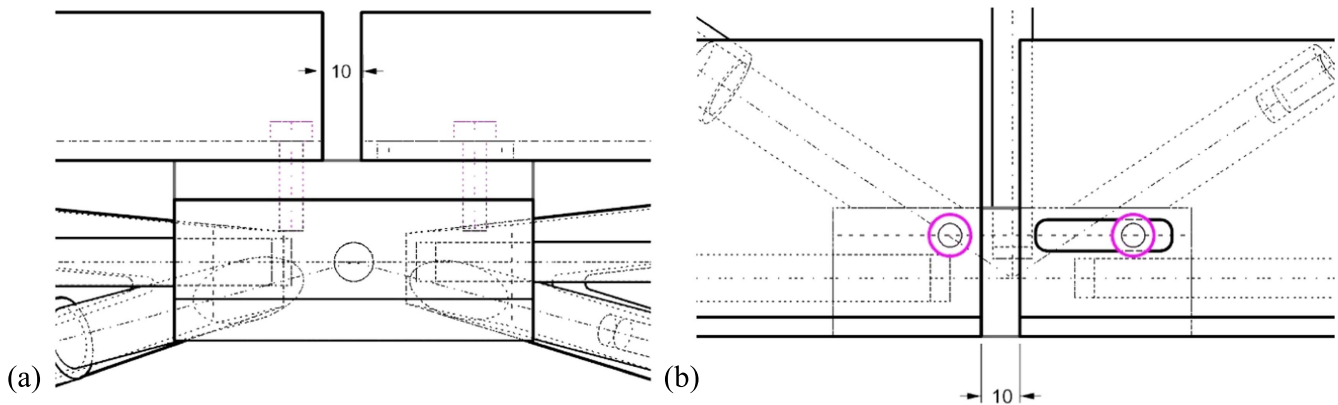


**Figure 11.** Deck to node connection; (a) top view; (b) front view.

actuators are sent via width modulation signals (PWM) to regulate the power needed to reach the target position. In addition, current sensors are installed at the mains supply to monitor the power used for shape control and all the other electronic devices part of the control system.

#### 4.1. Strain gauge based sensors

**4.1.1. Sensor architecture.** For the response to loading of any structural system to be identified and controlled the state of strains/stresses or a measure of its displacements must be known. For this reason, each element of the structure is fitted with a strain gauge-based sensor connected to form a Wheatstone bridge. A full-bridge configuration was chosen because it gives a sensitivity at  $1000 \mu\epsilon$  (microstrain) of circa  $1.3 mV_{out}/V_{EX}$  ( $V_{out}$  is the output voltage and  $V_{EX}$  the excitation voltage) which is the maximum obtainable compared with half and quarter bridge configurations. In addition, a full bridge compensates automatically for temperature drifts and lead resistance. The full-bridge configuration adopted here is of type 3 which is designed to

measure axial strains only and reject bending strains [33]. In this configuration four (or eight) active strain gauges are mounted on the specimen. Two (T1 and T2) measure tensile strains along the principal axis of strain and the other two (C1 and C2) are mounted transversely to measure the compressive Poisson effect. Figure 13 shows the gauges T1, T2 and C1, C2 arranged in strain rosettes to save space because the tie-bar have very small diameters (table 2).

In this bridge configuration, the voltage output is proportional to the sum of the change in resistance of the tensile gauges minus the sum of the change in resistance of the Poisson gauges.

Therefore, tensile strains due to bending cancel out giving the value for the axial strain. The strain  $\epsilon$  is given by:

$$\beta^e = \frac{-2V_r}{GF[(\nu + 1) - V_r(\nu - 1)]}, \quad (1)$$

where  $\nu$  is the Poisson ratio,  $V_r$  is the ratio between output and excitation voltage:

$$V_r = \frac{(V_{out(stained)} - V_{out(unstrained)})}{V_{EX}} \quad (2)$$

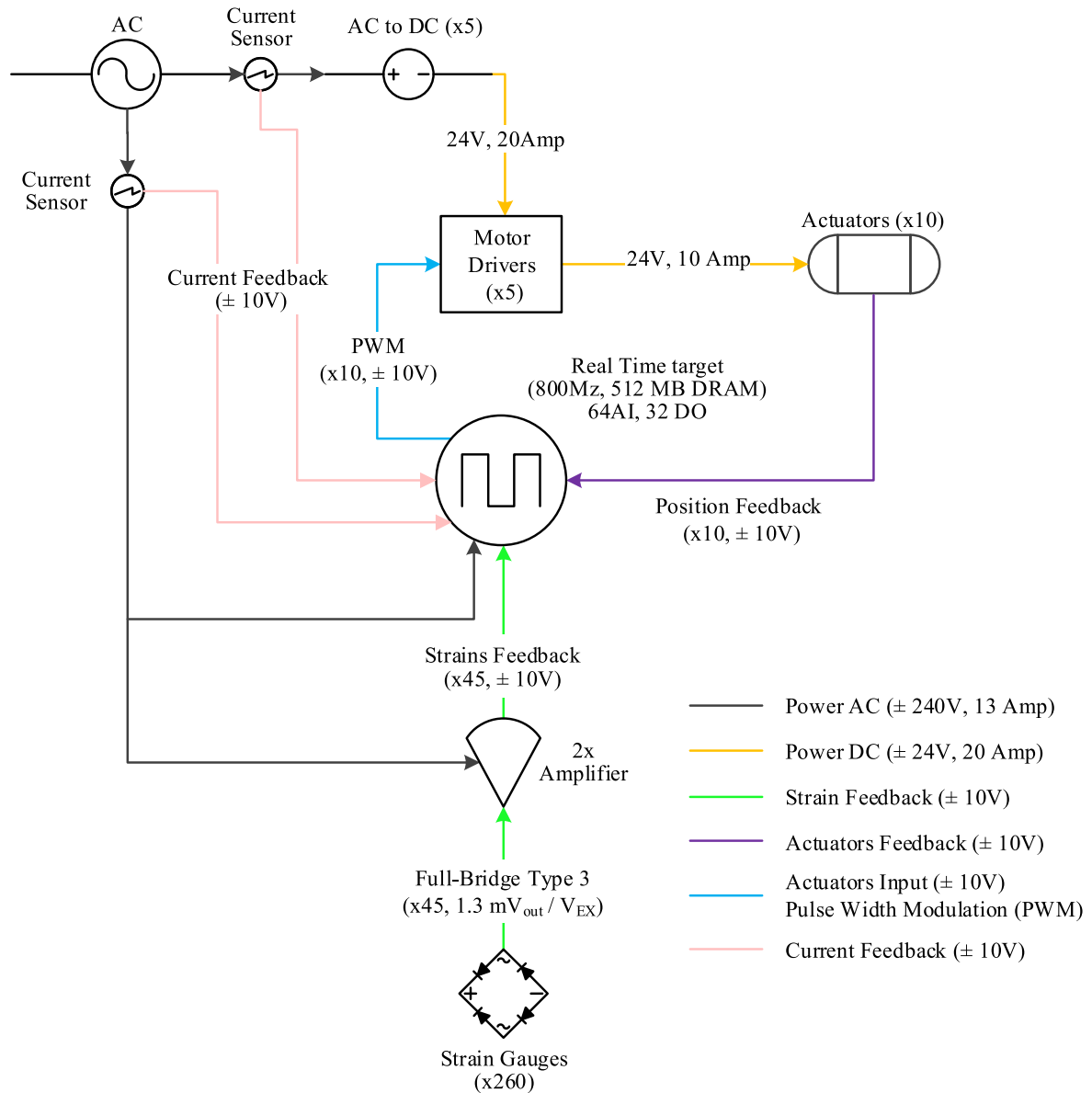


Figure 12. Control hardware architecture.

and the gauge factor  $GF$  is the ratio of fractional change in electrical resistance  $R$  to the strain  $\beta^e$ :

$$GF = \frac{\Delta R/R}{\Delta L/L} = \frac{\Delta R/R}{\beta^e}. \quad (3)$$

4.1.2. *Optimal sensor placement.* Rejection of bending strains is strongly dependent on the orientation of the bending moment with respect to the gauge position and the dimensions of the cross section. This is because although the gauges are supposed to be placed in diametrically opposite positions, misplacements will unavoidably occur during mounting, especially on a small cylindrical bar or tube. Figure 14 illustrates the gauges T1 and T2 positioned with a circular misplacement  $\varphi$  with respect to the  $y$ -axis. The red and blue triangles represent tension and compressive strains

induced by the moment (respectively),  $\theta$  the orientation of the bending moment.

The variation of the bending strain as a function of  $\theta$  is sinusoidal. The pink lines (figure 14) representing the distance from the neutral axis are  $\cos(\theta)$  and  $\cos(\theta + \varphi)$  for the strain readings at T1 and T2 respectively. The sum of the two strain readings at T1 and T2 position, plotted in figure 15(a), is the function:

$$\text{strain}(\theta) = \cos(\theta) - \cos(\theta + \varphi) \quad (4)$$

that has zero and maxima at:

$$\text{zero at } \theta = n\pi - \frac{\varphi}{2}; \quad \text{maxima at } \theta = n\pi - \left(\frac{\pi}{2} + \frac{\varphi}{2}\right). \quad (5)$$

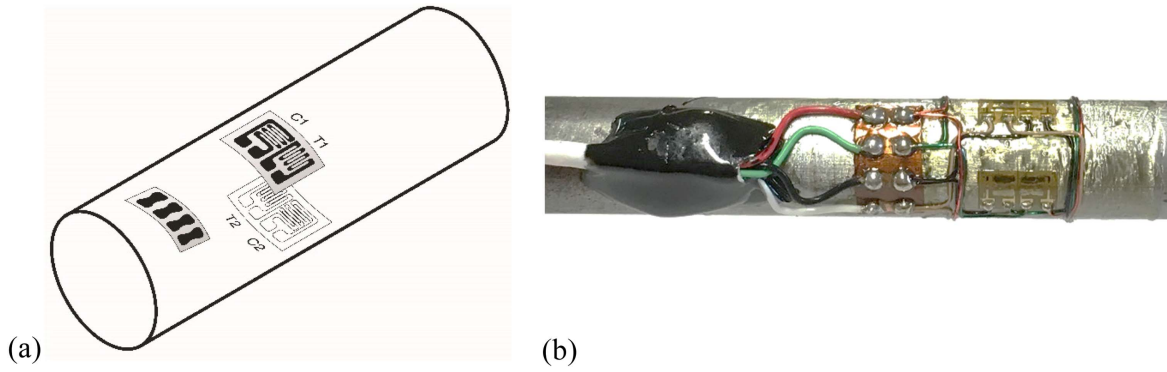


Figure 13. (a) Full bridge type 3; (b) sensor installed on 6 mm diameter bar.

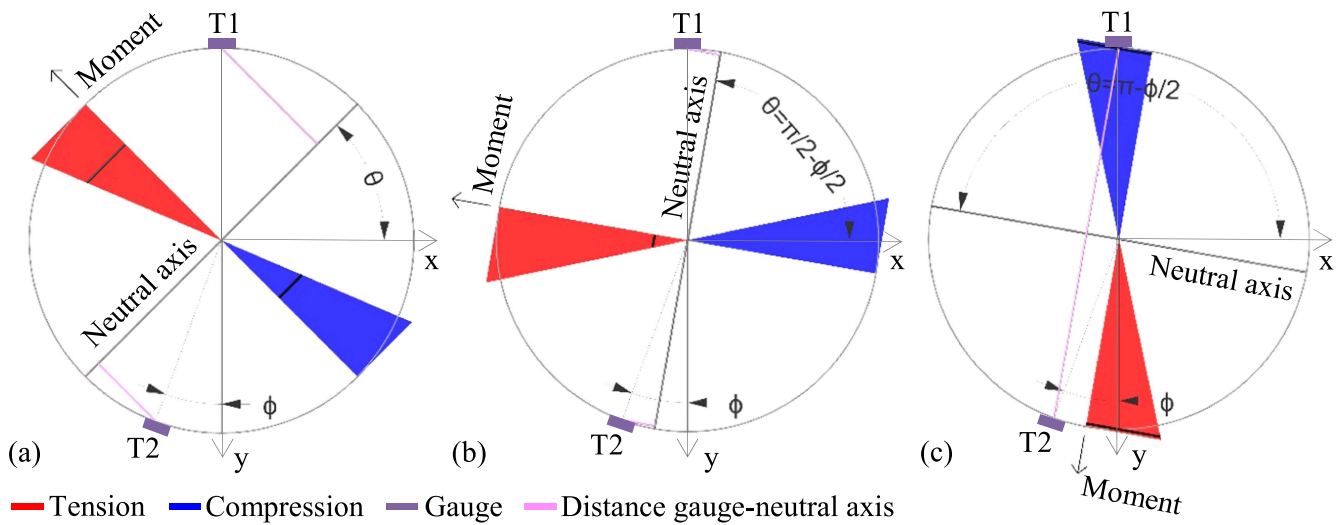


Figure 14. (a) Circular misplacement  $\varphi$ ; (b) max bending strain residual; (c) bending strain complete rejection.

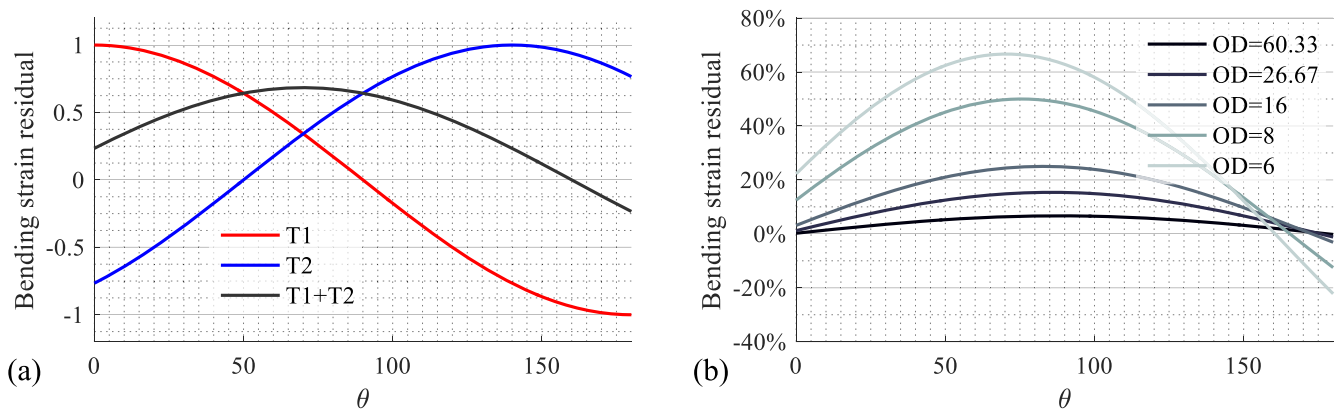


Figure 15. (a) Bending reading as a function of  $\theta$ ; (b) bending reading residual for bar with different outer dimensions (OD).

The readings cancel each other out only if the neutral axis happens to be orthogonal to the gauge placement axis ( $\theta = \pi - \varphi/2$ ) as shown in figure 14(c). For any other  $\theta$  the readings are not identical and therefore rejection of bending strains is not complete. The error reaches a maximum when the neutral axis is parallel to the gauge

placement axis ( $\theta = \pi/2 - \varphi/2$ ) because the readings are identical both in value and sign as shown in figure 14(b). The error due to gauge misalignment can become critical for small diameter elements. Assuming a chord misalignment of 2 mm (a tolerance given by the strain gauge installer), the angular misplacement  $\varphi$  becomes  $38.9^\circ$

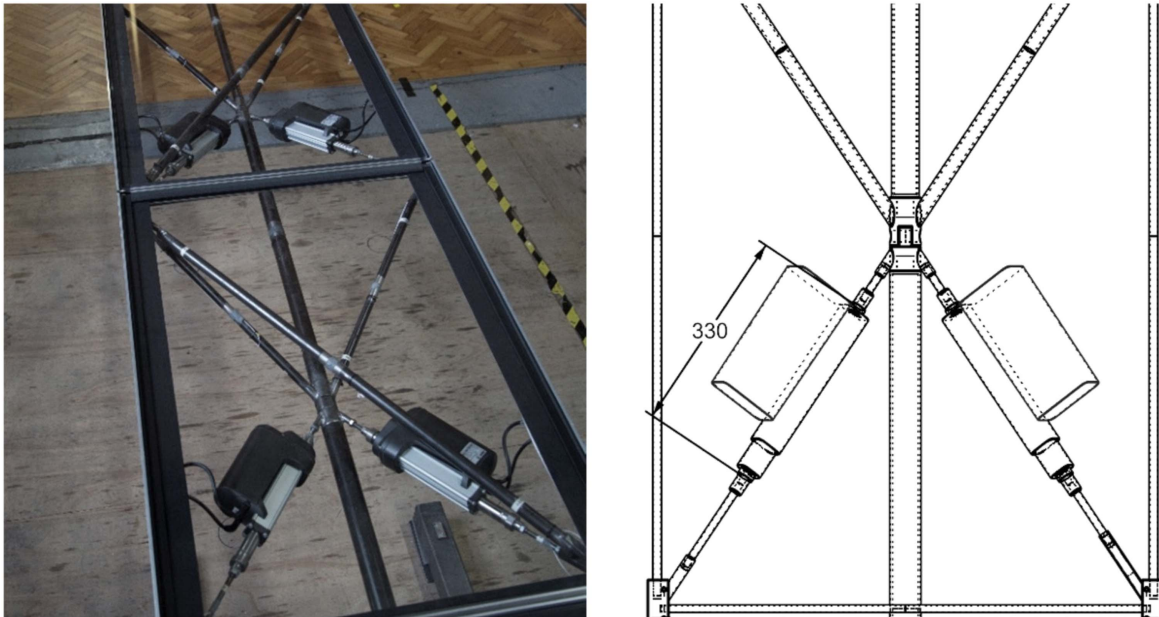


Figure 16. Actuator locations.

for 6 mm diameter bars resulting into a bending strain reading residual of 58% (thus achieving only 42% rejection) as shown in figure 15(b).

For this reason, a parametric study was carried out to estimate the effect of misalignment between the gauge axis and the neutral axis of a generic truss member. The optimal gauge axis (the placement axis) is that orientated at  $90^\circ$  with respect to the average neutral axis for the main design load cases. The error is obtained by normalising the value of the bending strain after rejection with that of the axial strain. This way it is possible to assess the relative contribution of the non-rejected bending strains on the axial strains. Since the load that is likely to occur the most is a medium weight person (75 kg) walking centrally along the truss, the main load case taken into consideration is set at 75% of the load case LC1. However, to account for the ‘one-sided’ load cases (LC2 and LC3) it is assumed that the neutral axis might typically deviate by 50% from that of the uniform load case (LC1).

This study confirmed that the orientation becomes critical for the top chord bracers (number 16–20, figure 7) because these elements experience lower levels of axial forces. The correction achievable by orienting the gauges gives an error reduction of 40% in this case. Similar case is for the 8 and 10 mm diameter tension diagonal bracers between top and bottom chords which experience significant bending due to the weight of the actuators. However, because these elements are connected to the nodes using left and right thread, it is not feasible to install the gauges at a specified orientation. For this reason, the tension diagonal bracers were fitted with an 8-gauge bridge (4 rosettes, 2 opposite facing pairs arranged at  $90^\circ$ ) which rejects bending strains more effectively.

There is a total of 260 strain gauges grouped into 45 full-bridge sensors (25 4-gauge and 20 8-gauge). During testing, it

was observed that a high level of noise in the strain signal was caused by electro-magnetic radiation emitted by the actuator motors. For this reason, the signal cables (figure 10(b)) are made of silver plated soft copper cores and are screened using silver plated soft copper braid [34].

**4.1.3. Actuators.** The actuator locations are determined selecting those elements whose length change contribute the most towards internal forces and displacements correction [30]. This analysis requires the selection of a certain number of degrees of freedom to be controlled (CDOFs). In this case, the CDOFs are the vertical displacements of all nodes of the top chords except the supports. The controlled nodes are indicated by spheres in figure 6(a). The minimum number of actuators  $n^{ACTs}$  to control exactly the required displacements is equal to the number of CDOFs  $n^{CDOFs}$  plus the degree of indeterminacy of the structure ( $n^{ACTs} = n^{CDOFs} + r$ ). Intuitively, this is the minimum number of actuators to turn the structure into a controlled mechanism. If fewer actuators are utilised, displacement control will only be partially achieved. Because the structure can be considered statically determinate ( $r = 0$ ), ten actuators are needed to control exactly the required displacements. In this case, a constraint was added to prevent the actuators from working in compression to avoid potential misalignment of the shaft. The resulting actuator locations are all the diagonal rod bracers. A coupler is placed at both ends of the actuator to join via threading with the round bars as shown in figure 16.

The choice of the actuators was informed by several factors including space constraints, weight requirements, low maintenance, force capacity and cost. The actuators adopted are electromechanical linear motors based on acme screw thread [35] each having a built-in potentiometer (0–10 V

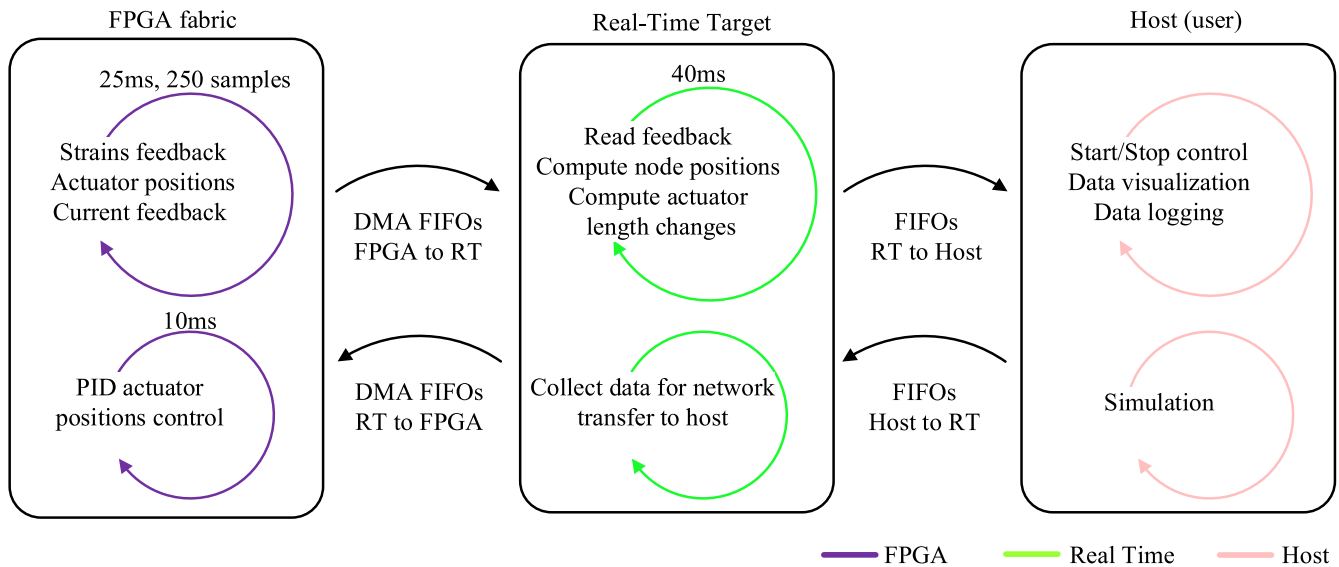


**Figure 17.** Control software architecture; real-time target (RT), field programmable gate array (FPGA), proportional-integral-derivative (PID) controller, direct memory access (DMA), first in first out (FIFO).

output) providing position feedback. One of the advantages of this type of actuator is that when power is cut off it remains locked in position which is important to guarantee the safety and serviceability of the structure. However, stroke velocities are limited because of friction in the spindle. These actuators have a maximum velocity of  $11 \text{ mm s}^{-1}$  at no load and  $7 \text{ mm s}^{-1}$  at max load  $-10 \text{ kN}$  both in tension and compression. The maximum expected length change is  $16 \text{ mm}$  for the actuators at the free end where control forces are the lowest. Conversely, for the actuators located at the constrained end, control forces are the highest (up to  $10 \text{ kN}$ ) but length changes are the smallest (up to  $5 \text{ mm}$ ). Note that the actuator response time is not quite fast enough for a proper dynamic control hence the quasi-static focus of the research at this stage.

**4.1.4. Control unit.** The control unit contains: the main controller—cRIO-9024 by National Instruments [36]; 5 control drivers each driving a pair of actuators—SD2130 by Roboteq [37]; 40-channel and 8-channel combined data acquisition system to amplify strain signals—FEMM-40 and FE-MM8 by Fylde [38]; 5 24 V DC power supplies each feeding a pair of actuators—GWS500 by TDK-Lambda [39].

The main controller is a low power (800 MHz, 512 MB DRAM) embedded real-time target machine. A real-time system is important to achieve deterministic control because it operates without buffering delays as well as minimal interrupt and thread switching latency. High latency might result in unwanted excitations of the structure caused by the actuators in the event of sudden changes of external loads.

Strain signals acquisition and control command input to the actuators are implemented on the integrated FPGA (field programmable gate array) fabric that comes with the controller. This way the computational load is distributed more efficiently. In addition, the FPGA logic-gates

arrangement can be optimised programmatically to perform a certain task generally running much faster than it would on a CPU.

## 5. Control software

### 5.1. Control software architecture

The control software can be divided in three main parts: acquisition, processing and visualisation. The real-time target runs the main control routine. Data visualisation, logging and simulation for comparison with theoretical predictions are implemented on the host computer (laptop or desktop computer). Figure 17 illustrates the architecture of the control software.

The acquisition and processing run asynchronously to guarantee smooth operational control. The acquisition of the strains, actuator stroke position feedback and electric current feedback is implemented using fixed-point arithmetic to utilise efficiently the FPGA computational resources which are limited compared to those of the CPU. In this way, it is possible to reach very high through-put and time deterministic reading. Every 25 ms a sample set made of 250 readings is taken from the 45 full-bridge strain sensors and the 10 actuator potentiometers. Values are averaged out for noise reduction and then transferred to the real-time target using DMA FIFOs (direct memory access, first in first out data buffer). The part of the algorithm that runs on the real-time target is computationally expensive due to usage of floating point arithmetic and linear algebra (e.g. matrix inversions). A full cycle comprising computation of displacements and actuator length changes takes about 40 ms. This means the structure is controlled at 25 Hz which is much higher than the 1st natural frequency of the system measured at 1.55 Hz.

Control commands are transferred via DMA FIFOs to the FPGA fabric which runs, asynchronously from the main

process, a fixed-point PID algorithm (proportional-integral-derivative controller) to drive the actuators to target positions. To keep power consumption to a minimum, a switch on/off command is sent to the actuator driver to cut off power supply as soon as the target position is reached.

## 5.2. Control algorithm

**5.2.1. Main steps.** The main part of the control algorithm is based on the method given in Senatore [30] and outlined here in section 2. The control algorithm is given here for the general case addressing both statically determinate and indeterminate structures. A single cycle ( $t, t + \Delta t$ ) can be divided in four main steps:

1. Compute the force difference vector  $\Delta \mathbf{F}(t)$  between the compatible forces  $\mathbf{F}^{\text{COMP}}(t)$  and the optimal ones  $\mathbf{F}(t)$  achieved via actuation (i.e. load path redirection);
2. Compute node displacements  $\mathbf{u}(t)$  from strain values and actuator stroke positions to obtain the displacement difference vector  $\Delta \mathbf{u}(t)$ —difference between current and required node positions;
3. Compute the actuator length change vector  $\Delta \mathbf{L}(t + \Delta t)$  to compensate for forces  $\Delta \mathbf{F}(t)$  and displacements  $\Delta \mathbf{u}(t)$ ;
4. Compute the actuator target position at  $t + \Delta t$ .

During control, the distinction between compatible  $\mathbf{F}^{\text{COMP}}(t)$  and optimal load path  $\mathbf{F}(t)$  is useful to distinguish the internal forces before and after the actuator length changes  $\Delta \mathbf{L}(t + \Delta t)$ . In practice, for a real structure working within the material elastic limit, the load path is always a compatible one. The compatible forces  $\mathbf{F}^{\text{COMP}}(t)$  can be thought of as the superposition of the internal forces caused by the external load at time  $t$  with no actuation and those resulting after the actuator compensation at time  $t - \Delta t$ . In other words, the load path is redirected at each update moving through different optimal states via shape changes until the displacements are reduced within required limits.

**5.2.2. Load path redirection.** The element strain vector  $\beta^e(t)(n \times 1)$  is obtained from the voltage outputs given by the strain gauge sensors as defined in equation (1). Once the strain vector is known it is used to obtain the compatible force vector:

$$\mathbf{F}^{\text{COMP}}(t) = \mathbf{E} \cdot \beta^e(t) \cdot \alpha, \quad (6)$$

where  $\mathbf{E}(n \times 1)$  is the Young's modulus vector and  $\alpha(n \times 1)$  the vector of cross section areas. The optimal load path  $\mathbf{F}(t)$  can only be derived if the external load vector  $\mathbf{P}(t)$  is known. Note that no assumption has been made on direction, position and magnitude of the external load. Using the integrated force method [40] the external load vector can be computed as:

$$\begin{bmatrix} \mathbf{B}^{\text{RED}}(t) \\ \mathbf{C}(t) \cdot \mathbf{G}(t) \end{bmatrix} \cdot \mathbf{F}^{\text{COMP}}(t) = \begin{bmatrix} \mathbf{P}^{\text{RED}}(t) \\ \mathbf{P}^{\text{EIG}}(t) \end{bmatrix} = \mathbf{P}^*(t), \quad (7)$$

where  $m$  is the number of degrees of freedom,  $\mathbf{B}^{\text{RED}}(t)[(m - n^R) \times n]$  the equilibrium matrix reduced to the unconstrained degrees of freedom,  $\mathbf{C}(t)(r \times n)$  the compatibility matrix containing the  $r$  (degree of static indeterminacy) states of self-stress and  $\mathbf{G}(t)(n \times n)$  the flexibility matrix. The compatibility matrix  $\mathbf{C}$  can be obtained directly from the equilibrium matrix  $\mathbf{B}^{\text{RED}}$  by computing its null space via singular value decomposition which gives the  $r$  states of self-stress vector:

$$\mathbf{C} = \text{null}(\mathbf{B}^{\text{RED}})^T. \quad (8)$$

The load vector is made of two components: (1)  $\mathbf{P}^{\text{RED}}(t)[(m - n^R) \times 1]$  the external load vector reduced to the unconstrained degrees of freedom and  $\mathbf{P}^{\text{EIG}}(t)(r \times 1)$  is defined here as the eigenstrain load vector associated with geometrical incompatibilities. The eigenstrain load vector complements the external load vector offering a way to set directly the length change of the actuators:

$$\mathbf{P}^{\text{EIG}}(t) = -\mathbf{C}(t) \cdot \beta^0(t) \cdot \mathbf{L}, \quad (9)$$

$$\beta^0(t) = \frac{\Delta \mathbf{L}(t)}{\mathbf{L}}, \quad (10)$$

where  $\mathbf{L}(n \times 1)$  is the element length vector,  $\Delta \mathbf{L}(t)(n \times 1)$  the actuator length change vector and  $\beta^0(t)(n \times 1)$  the non-elastic part of the total strain which is referred as *eigenstrain* in some of the residual-stress literature [41–43]. Eigenstrain distribution is normally produced by thermal, plastic, creep strain or lack of fit but here it is thought of as caused by the actuator length changes. The vector  $\Delta \mathbf{L}(t)$  can be computed with respect to the previous time step or to the initial position for geometric nonlinear control or linear geometric control respectively:

$$\Delta \mathbf{L}(t) = \begin{cases} \mathbf{x}^{\text{ACTs}}(t) - \Delta \mathbf{L}^0 & \text{if linear geometric} \\ \mathbf{x}^{\text{ACTs}}(t) - \mathbf{x}^{\text{ACTs}}(t - \Delta t) & \text{if non-linear geometric,} \end{cases} \quad (11)$$

where  $\mathbf{x}^{\text{ACTs}}(t)(n \times 1)$  and  $\mathbf{x}^{\text{ACT}}(t - \Delta t)(n \times 1)$  are the current and previous time step position of the shaft of the actuators and  $\Delta \mathbf{L}^0$  is the initial position of the actuators at  $t = 0$ . Because the actuator length change vector  $\Delta \mathbf{L}(t)$  is known, so is the eigenstrain load vector  $\mathbf{P}^{\text{EIG}}(t)$  (equation (9)), and therefore the only unknown term in equation (7) is the reduced external load vector  $\mathbf{P}^{\text{RED}}(t)$  which can be found by extracting the first  $(m - n^R)$  component of the load vector  $\mathbf{P}^*(t)$ .  $\mathbf{P}(t)$  is then obtained by solving force-equilibrium at the supports. Once the external load  $\mathbf{P}(t)$  is known the optimal load path  $\mathbf{F}^{\text{EXT}}(t)$  (including support reactions) can be computed:



Figure 18. (a) Load test; (b) node displacement measurement.

$$\begin{cases} \min_{\mathbf{F}} \|\mathbf{F}^{EXT}(t)\|^2 \\ \text{s.t.} \\ \mathbf{A}^{EQ}(t) \cdot \mathbf{F}^{EXT}(t) - \mathbf{P}(t) = 0, \\ \mathbf{A}^{ULS}(t) \cdot \mathbf{F}^{EXT}(t) - \boldsymbol{\alpha} \leq 0 \\ \mathbf{A}^{ULSB}(t) \cdot \mathbf{F}^{EXT}(t) - \boldsymbol{\alpha} \leq 0 \end{cases} \quad (12)$$

Equation (12) finds the optimal forces subject to satisfying equilibrium constraints  $\mathbf{A}^{EQ}(t)$  as well as a set of inequality constraints to account for ULSs (admissible stress  $\mathbf{A}^{ULS}(t)$  and buckling  $\mathbf{A}^{ULSB}(t)$ ) [30]. The problem stated in Equation (12) can be solved using sequential quadratic programming. Once the optimal force vector  $\mathbf{F}(t)$  is known, the force difference vector  $\Delta\mathbf{F}(t)$  follows immediately:

$$\Delta\mathbf{F}(t) = \mathbf{F}(t) - \mathbf{F}^{COMP}(t). \quad (13)$$

Note that for statically determinate structures and without considering geometric nonlinearity, the actuator length changes do not cause change in the strain/stress. Compatible and optimal forces are the same  $\mathbf{F}^{COMP}(t) = \mathbf{F}(t)$  hence there is no need to redirect the load-path to enforce compatibility. However, shape changes are still required to satisfy required deflection limits.

**5.2.3. Shape control.** The node displacement vector  $\mathbf{u}(t)$  is computed from the equilibrium matrix  $\mathbf{B}^{RED}(t)$ , the compatibility matrix  $\mathbf{C}(t)$  and the actuator length change vector  $\Delta\mathbf{L}(t)$ :

$$\mathbf{u}(t) = \mathbf{J}(t) \cdot \{\mathbf{G}(t) \cdot \mathbf{F}(t) + \Delta\mathbf{L}(t)\}, \quad (14)$$

where  $\mathbf{J}(t)[(m - n^R) \times n]$  is the deformation coefficient matrix defined in the IFM [40]:

$$\mathbf{J}(t) = \text{first } (m - n^R) \text{ rows of } \left[ \begin{bmatrix} \mathbf{B}^{RED}(t) \\ \mathbf{C}(t) \cdot \mathbf{G}(t) \end{bmatrix}^{-1} \right]^T. \quad (15)$$

The displacements vector  $\mathbf{u}(t)$  is then used to compute  $\Delta\mathbf{u}(t)$ :

$$\Delta\mathbf{u}(t) = \mathbf{u}^{SLS}(t) - \mathbf{u}(t), \quad (16)$$

where  $\mathbf{u}^{SLS}(t)$  is the vector of required displacements for the controlled degrees of freedom. The required displacements are set using constraints on the curvature between adjacent nodes to ensure smooth shape changes, and prevent damage to the deck/cladding at any stage of the control process [30].

**5.2.4. Update actuator stroke positions.** The actuator stroke positions are updated by computing the length change  $\Delta\mathbf{L}(t + \Delta t)$  to compensate for the force difference vector  $\Delta\mathbf{F}(t)$  and the displacement difference vector  $\Delta\mathbf{u}(t)$ . The problem is formulated as a constrained minimisation:

$$\begin{cases} \min_{\Delta\mathbf{L}} \|\mathbf{S}^{u|RED} \cdot \Delta\mathbf{L}^{RED}(t + \Delta t) - \Delta\mathbf{u}^{RED}(t)\|^2 \\ \text{s.t.} \\ \mathbf{S}^{F|RED} \cdot \Delta\mathbf{L}^{RED}(t + \Delta t) = \Delta\mathbf{F}(t) \end{cases}, \quad (17)$$

where  $\mathbf{S}^{u|RED}(n^{CDOFs} \times n^{ACTs})$  and  $\mathbf{S}^{F|RED}(n \times n^{ACTs})$  are the reduced displacement and force sensitivity matrix respectively. The problem stated in equation (17) can be solved using generalized singular value decomposition. This method produces a minimum norm solution even when the constraint matrix is rank deficient. The full size displacement and force sensitivity matrices store the effect of a unit length change of each element on nodal displacements ( $\mathbf{S}^u$ ) and axial forces ( $\mathbf{S}^F$ ) of the other elements respectively [30]. These matrices are used to obtain the actuator layout as described in [30]. When used for control, these matrices must be reduced (hence the superscript RED) by extracting the  $n^{ACTs}$  columns corresponding to the actuators. In addition,  $\mathbf{S}^u$  and  $\Delta\mathbf{u}$  must be



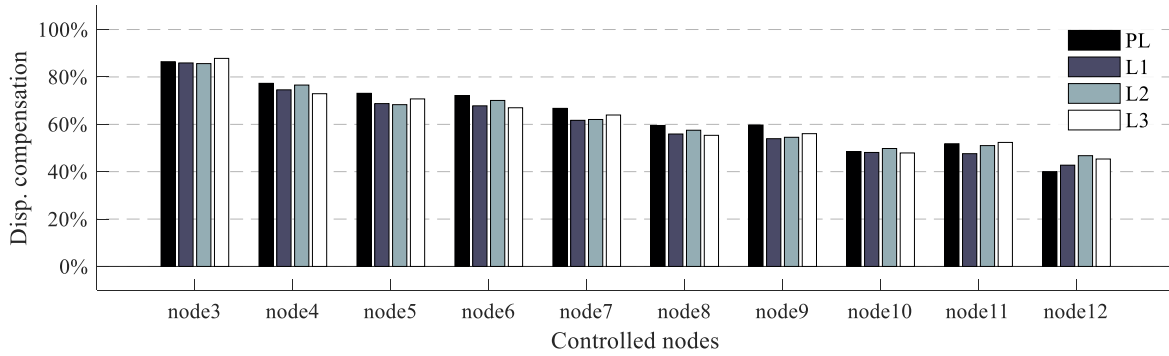


**Figure 19.** Displacement compensation under permeant load (PL) and live load cases (L1 to L3).

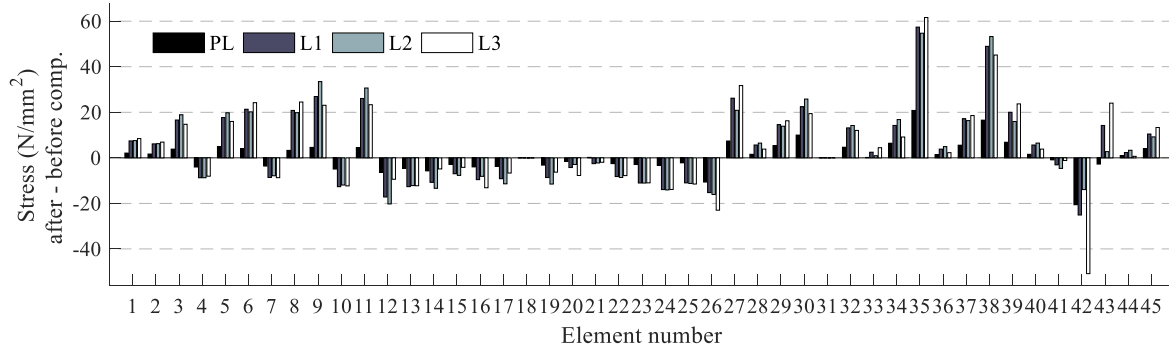


**Figure 20.** Stress after minus stress before displacement compensation under permeant load (PL) and live load cases (L1 to L3).

further reduced by extracting the rows corresponding to the controlled degrees of freedom. This way the rank of the reduced matrices  $S^{u|RED}$  and  $S^{f|RED}$  is in general equal to  $n^{CDOFs}$  and  $r$  respectively and their sum is  $n^{ACTs}$  which is the size of the vector of the unknown variables  $\Delta L^{RED}(n^{ACTs} \times 1)$ .  $\Delta L^{RED}$  is obtained from  $\Delta L$  reduced to the non-zero components corresponding to the actuator stroke positions. For statically determinate structure layouts,  $\Delta L^{RED}$  is obtained directly using the pseudo-inverse of the reduced displacement sensitivity matrix:

$$\Delta L^{RED}(t + \Delta t) = (S^{u|RED})^+ \cdot \Delta u^{RED}(t). \quad (18)$$

Once  $\Delta L(t + \Delta t)$  is known the target actuator stroke positions are computed using a forward step:

$$x^{ACTs}(t + \Delta t) = \Delta L(t + \Delta t) + x^{ACTs}(t). \quad (19)$$

## 6. Experimental programme

Experimental measurements carried out on the prototype had two main objectives: (1) to test whether it is possible to keep displacements within required limits via real-time shape changes with no prior knowledge of the direction, position and magnitude (within limits) of the external load; (2) to provide actual measurements of the operational energy consumed for structural adaptation so that numerical simulations can be realistically calibrated and confirmed.

Load tests were carried out by placing weights ranging from 10 kg to 140 kg using a cable lift stacker shown in

figure 18(a) or by a person walking on the deck. In both cases, displacements were measured using a self-levelling laser [44] which has an accuracy of 2 mm over 30 m. A probe was used to measure the distance between the nodes and the laser beam as shown in figure 18(b). To ensure measurement repeatability, the probe's end is a 5 mm diameter ruby ball which matches with a conical recess made on the top face of each node. To monitor power consumption, current metres are installed on the mains supply. The current metre is a Hall-effect based sensor which returns a voltage within 0–5 V proportional to the current intensity [45].

### 6.1. Experimental results

**6.1.1. Displacements control.** The maximum allowed displacement for any of the controlled nodes was set to 0 (i.e. total compensation) within a tolerance of  $\pm 2$  mm to find out whether 'infinite stiffness' could be achieved. 'Infinite stiffness' is here understood as reducing practically to zero displacements under loading without implying the structure becomes rigid. Controlled degrees of freedom were defined in 4.1.3 and controlled nodes are indicated in figure 6(a). The displacements were measured before and after shape control. Figure 19 shows the bar chart of the difference between the displacements before and after shape control divided by the displacements before shape control at the controlled nodes for each load case. These measurements showed that the displacements of nodes closer to the fixed end were reduced by 80% and those at the free end by only 40%.

The main cause for this discrepancy was due to the deformation of the support frame onto which the truss is

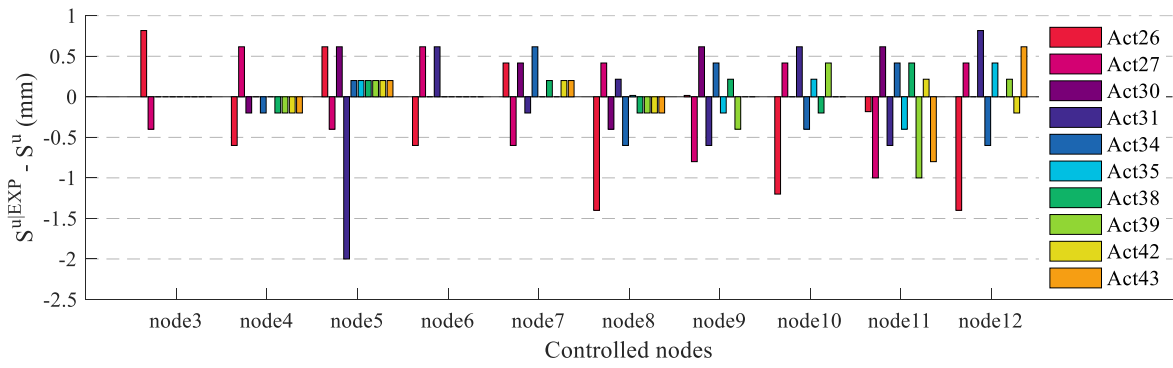


Figure 21. Difference between measured and predicted displacements caused by actuator unit length change.

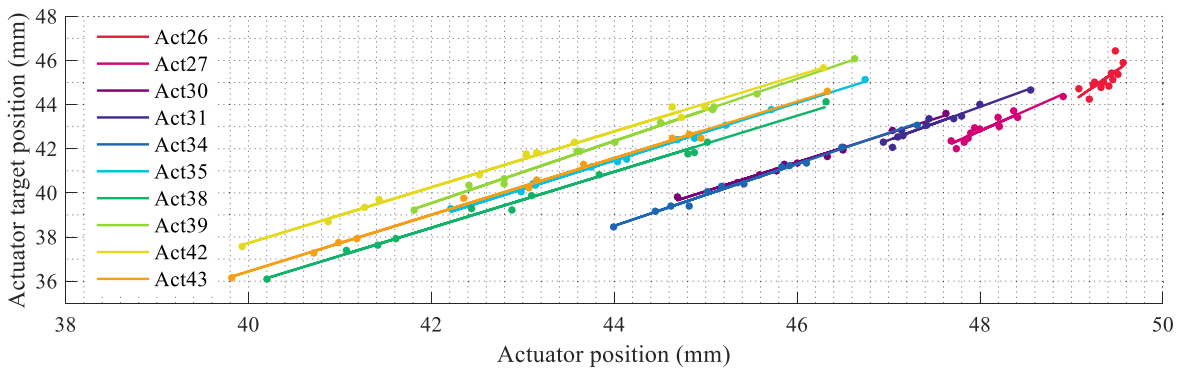


Figure 22. Actuator target positions versus measured positions under live load L1.

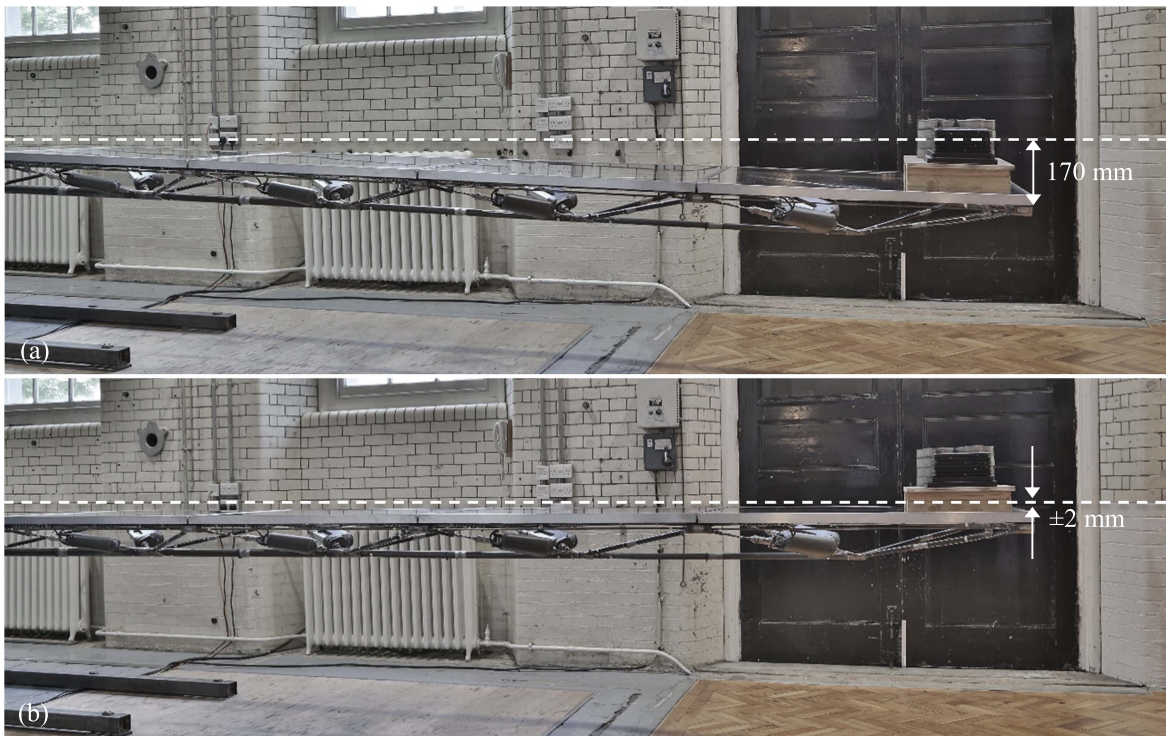


Figure 23. (a) 100 kg before control; (b) 100 kg after control.

pinned. Clearly, the final node position depends on whether the ‘fixed’ nodes (those pinned at the support frame) do not move or move very little. Due to a 6:1 ratio between the length of the cantilever (6000 mm) and the height of the

upright frame, a very small rotation of the support frame amplifies into a significant displacement at the free end.

Discrepancies were also measured between the element stress before and after displacement compensation. As



**Figure 24.** Person (70 kg) walking, comparison deformed (transparent) and controlled shape.

expected, since the truss is not a perfectly pin-jointed structure, the element stresses are affected by the actuator length changes during shape control. Figure 20 shows the difference between the stress measured after and before shape control in each element and load case. The difference is high for the diagonal solid bars that couple with the actuators (e.g. elements 27, 35, 38, 42) and the elements of the last bay because of residual deformation developed during welding.

The combined effect caused by the deformation of the support frame and the discrepancy between measured and predicted element stress was mitigated by calibration based on correlation. The calibration process consists of two main steps: (1) build an experimental displacement sensitivity matrix  $S^{u|EXP}$ ; (2) find an empirical function that corrects the predicted actuator length changes to achieve the required displacement compensation.

The experimental displacement sensitivity matrix was obtained recording node displacements caused by a unitary length change of each actuator in turn (section 5.2.4). Figure 21 shows the difference between the measured displacements and the predicted ones caused by each actuator unitary length change. On average, the discrepancy tends to be higher for each actuator the closer the node to the free end. Using the experimental sensitivity matrix, it was possible to reduce displacement over-compensation for the nodes closer to the fixed end. However, there was little improvement reducing the node displacements at the free end. This confirmed further the main issue was the support frame deformation causing a rigid-body rotation of the truss.

To eliminate the effect of the support frame deformation, additional actuator length changes were programmed in so both the rigid body rotation and the displacements due to the truss deformation were compensated for each load test. This way, a correction function was found between the actuator length changes as given by the control routine explained in section 5.2.4 and the target ones. Figure 22 shows the relation between predicted and target actuator length changes under live load L1. Similar measurement were recorded

under the asymmetric load cases. Because the relationships are practically linear, least square regression was sufficient to find a correction function for each actuator. However, using nonlinear regression based on kernel methods (supervised learning) [46], in this case using a Gaussian kernel, it was possible to generalise better for the asymmetric load cases.

The implementation of the correction function adds a step to the control algorithm:

$$\Delta L(t + \Delta t)^* = f(\Delta L(t + \Delta t)), \quad (20)$$

$$\mathbf{x}^{ACTs}(t + \Delta t) = \Delta L(t + \Delta t)^* + \mathbf{x}^{ACTs}(t), \quad (21)$$

where  $\Delta L(t + \Delta t)^*$  is the vector of target actuator length changes and  $f$  the correction function.

Figure 23 shows the deformed shape without control (a) and the controlled shape (b) achieved after calibration. Measurements showed that displacements of controlled nodes were practically reduced to zero for both symmetric and asymmetric loads thus achieving an effective ‘infinite stiffness’. The difference in the vertical position of two consecutive nodes was within  $\pm 1$  mm and between supports and free end nodes within  $\pm 3$  mm. When the load is applied at the free end, the bottom chord takes a curved profile i.e. the depth of the bays reduces from the fixed to free end.

Displacement control tests were also carried out under a moving load i.e. a person walking on the deck at moderate speed to avoid potential dynamic amplification issues. Also for this case deflections were practically reduced to zero. When a person walks on the deck, the actuators change length continuously to compensate for displacements as the load changes position. Figure 24 shows a comparison between the deformed (transparent) and controlled shape under moving load. Demonstration movies are available online [47].

**6.1.2. Power consumption|total energy assessment.** The structure was designed to take a permanent load as well as a randomly changing live load as described in 3. The statistics of this live load were modelled using a Log-Normal probability distribution because it is closely related to the

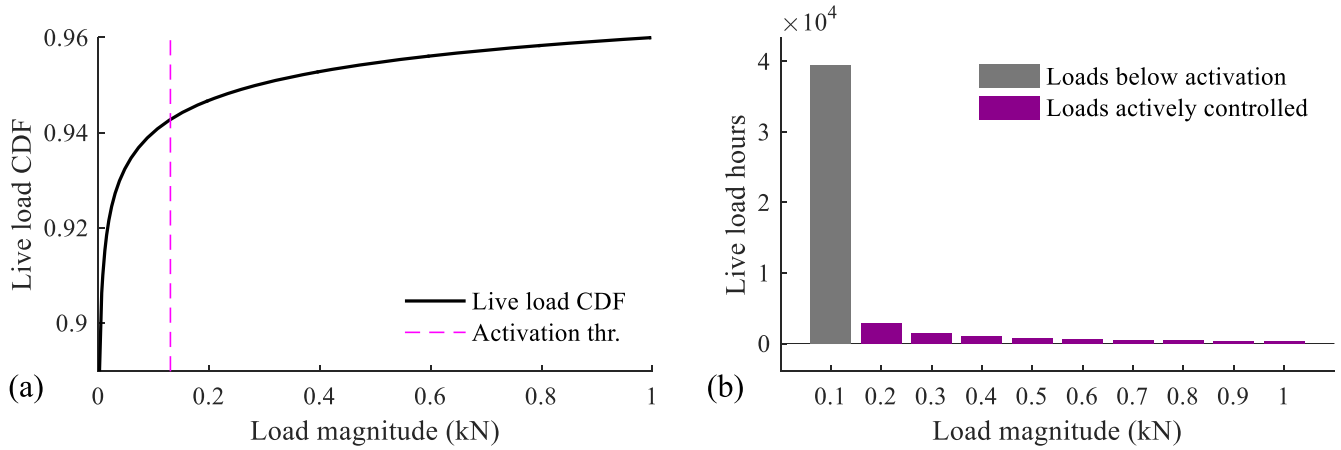


Figure 25. (a) Live load CDF; (b) live load hours.

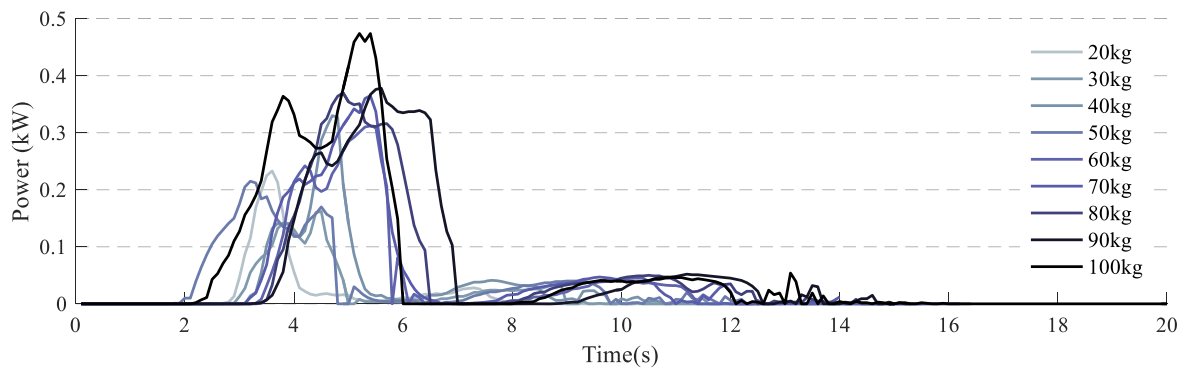


Figure 26. Power measurement.

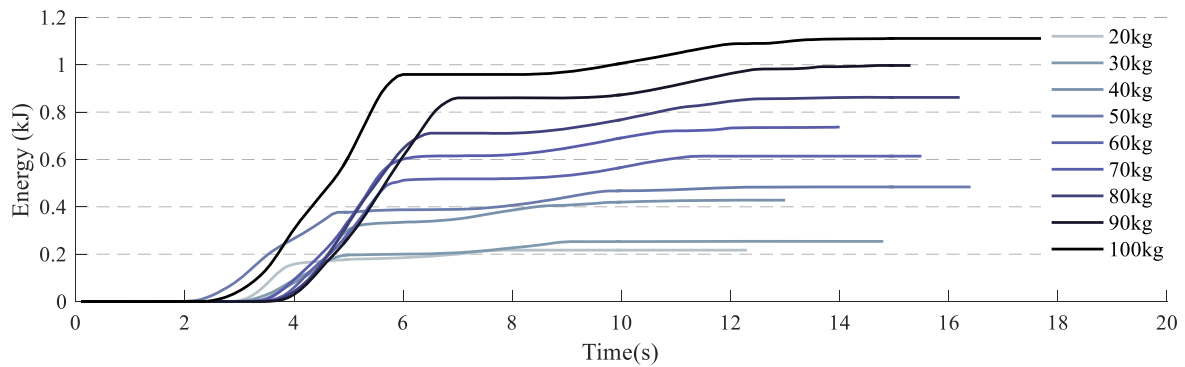


Figure 27. Energy measurement.

Normal probability distribution, hence it is general, only taking positive real values and thus providing the required bias toward the lower values of the random variable. The design load (excluding safety factor), thereafter called the characteristic load is defined as the 95th percentile of the load probability distribution. The probability distribution only describes the occurrence of the live load. For simplicity, the mean of the underlying normal distribution is set to zero. Once the mean and the characteristic load are set, the standard deviation is adjusted so that the design load corresponds to the 95th percentile. To calculate the total energy consumed throughout the life of the structure a design life must be

assumed. The structure is assumed to be designed for 50 years.

Deflection limits were set to span/500 (12 mm) which is normally used as serviceability criteria for the total drift of a building subjected to wind loading [48]. The reason why the adaptive truss spans horizontally is due to space constraints and ease of construction. However, due to its slenderness the truss can be thought of as a scaled version for the super structure of a tall tower subjected to wind load.

Figure 25(a) shows the live load cumulative distribution function and the activation threshold indicated by a dashed line. This was predicted at 0.15 kN and it was measured at

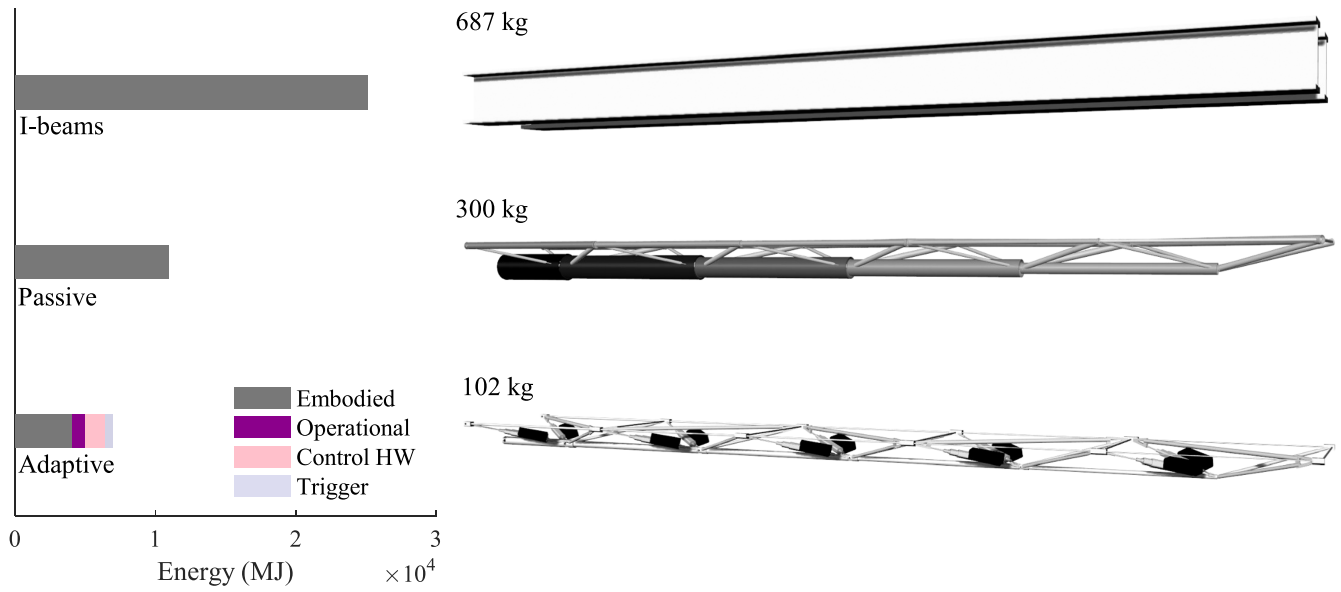


Figure 28. Energy comparison I-beams versus optimised passive structure versus adaptive structure.

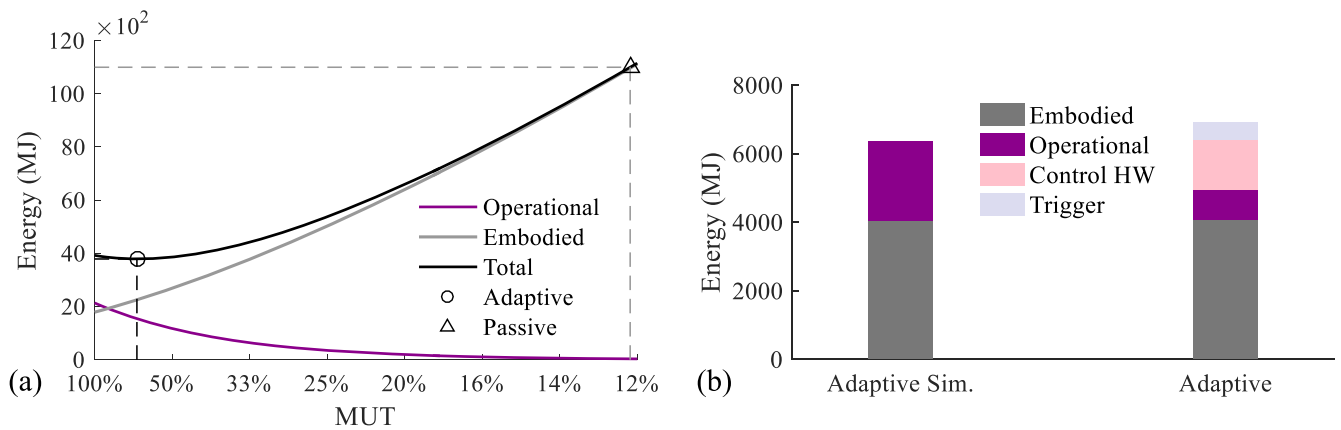


Figure 29. (a) Energy curves versus MUT; (b) total energy prediction versus measurement.

0.14 kN, hence for all the loads below 0.14 kN the end deflection will be within required limits. Figure 25(b) shows the number of hours of each occurrence of the live load whose distribution is divided in 10 steps from 10 kg to 100 kg. The total number of hours above the activation threshold amounts to 1 year approximately.

Power consumption was recorded for all electronic devices including the actuation system, signal conditioning and main control processor. The power was recorded during displacement compensation of the live load only. The permanent load was compensated by an initial shape change. Each load (10 kg to 100 kg) was placed on the deck between node 11 and node 12 (node labels are given in figure 6). The structure immediately adapted to the load. Once the displacements were reduced within limits, power was automatically cut off. Figure 26 shows the power consumption curves obtained from the measurements. The curves are consistent and repeatable over several measurements even if the cable lift stacker was manually operated. The power curves show a first peak upon application of the load (around 5 s) and then a lower peak upon release of the load (around

10 s). This is because when the live load is removed, the shape change to compensate for displacements caused by the permanent load requires the actuators to expand under tensile forces and thus very little power is needed. Energy is still consumed because the actuators used in this prototype change length via a lead screw mechanism. In theory there is a release of energy (i.e. the work is negative) that could be potentially harvested by using a different actuation technology (e.g. hydraulics) and an energy accumulator.

Figure 27 show the total energy consumed over time for each load test. Depending on the magnitude of the load, it took on average 4 s upon application and 2 s upon release until power was automatically cut off after the controlled node displacements reached the required limit.

The total operational energy was computed by multiplying the energy consumption by the live load hourly distribution for all load levels above the activation threshold. The total energy of the adaptive truss prototype is benchmarked against the embodied energy of two passive structures shown in figure 28. These structures are designed to comply with the same deflection limits and are subjected to

the same loads the adaptive truss was designed for. The first structure is made of two steel I-beams with a depth 220 mm and total weight of 687 kg. The second is an equivalent truss designed using a method described in [30] which produces designs comparable with or outperforming the Modified Fully Utilised Design [49]. Figure 28 shows the comparison between the embodied energy of the I-beams, that of the passive optimised truss and the total energy of the adaptive truss. The adaptive truss achieves 70% total energy savings compared to the I-beams and 40% compared to the passive optimised truss.

The energy analysis is carried out using a material energy intensity factor to convert the material mass into embodied energy. The material utilised in the simulations described in this paper is steel in the form of rods obtained from predominantly virgin materials (no recycled content) whose energy intensity is  $35 \text{ MJ kg}^{-1}$  [50]. Improvements in material production might change this value in the future. However, to reach a break-even point so that there would be no energy saving with respect to the I-beams and the optimised passive truss, the energy intensity must reduce by 87% ( $4.75 \text{ MJ kg}^{-1}$ ) and 60% respectively.

The adaptive truss total energy is broken down in four terms: (1) the embodied energy in the material mass of the structure which includes that of the actuators; (2) the operational energy to power the actuators during displacement compensation; (3) a constant term to power the control hardware for the loads above the activation threshold; (4) the operational energy to power a so called ‘trigger’ sensor. This is a sensor whose function is to detect anomalous movement and switch on power to the control system. This sensor must require low power because it is the only electronic device that must stay active during the entire life span of the structure. For this prototype an LVDT would be adequate (average consumption is 0.16 W) [51]. For larger scale structures, other methods could be considered (e.g. GPS, close-range photogrammetry).

Figure 29(a) shows the variation of the operational and embodied energy as the material utilisation factor varies. The adaptive solution was found for an  $\text{MUT} = 66\%$  whilst the passive solution corresponds to an  $\text{MUT} = 12\%$ . This means that the optimised adaptive and passive structures are designed so that the maximum stress under the worst load combination is 66% and 12% of the yield stress respectively. Figure 29(b) shows the difference between the operational energy predicted via simulation and the operational energy computed from measurements. Total energy savings were predicted as 42% with respect to the optimised truss rather than 37% as obtained from the measurements. The measured operational energy for the actuators is only 40% of that predicted via the simulation. The former was overestimated because it was assumed that the actuators always work at a fixed frequency equal to the first natural frequency of the structure. However, the energy it takes to power the control hardware was ignored (control HW in the legend of figure 29(b)) which is instead a significant part of the operational energy. The control hardware energy is part of the total operational energy but it is not related to the energy

needed for structural adaptation which is usually substantially higher. The control hardware energy requirement becomes important for small structures because in this cases it is comparable with the embodied energy savings.

Considering that the measured value of the operational energy was lower than that that predicted from the simulation, this experiment confirmed that the design method given in Senatore *et al* [30] is reliable producing results that are overall conservative.

## 7. Conclusions

Adaptive structures offer an emerging design paradigm that deals with providing stiffness in a completely different way to traditional engineering. Whilst the strength of the structure cannot be obviously compromised, trade-offs on the stiffness can be investigated. If the structure relies on an active system for deflection control, its stiffness can be modified strategically such that the passive-active configuration achieves higher efficiency in terms of whole-life energy.

The prototype structure described in this paper has shown that adaptive structures can achieve very high degree of slenderness—in this case the ratio span-to-depth is 37.5:1 which is much higher than that achieved using conventional structural solutions ( $\sim 12:1$  conventional trusses and 20:1 for conventional steel beams). The prototype structure is extremely light-weight—the frame without actuators and deck weighs only 52 kg.

Experimental results showed that displacement control was achieved within a tolerance of  $\pm 2 \text{ mm}$  between the fixed end and the free end of the cantilever thus achieving an effective ‘infinite stiffness’ (i.e. practically zero displacements under loading). Measurements showed that the operational energy for shape control for the entire life span of the structure is in good accordance with the results produced by numerical simulations. This result confirms the reliability of the design method proposed in Senatore *et al* [30] and crucially that adaptive structure achieve substantive total energy savings compared to passive structures.

Some considerations on scaling can be given. The energy consumption related to the control hardware (excluding the term for structural adaptation) does not necessarily scale with the size of the structure. For instance, if the geometry of the truss was to double in all dimensions, the energy term related to the control hardware will be similar because the same control system could be used again. In this case the operational energy needed for structural adaptation will increase substantially, becoming dominant with respect to the control hardware share.

This prototype was also built as a demonstration piece to show in a practical and interactive way the potential of the underlying design methodology to professionals in the field—structural engineers, architects, fabricators. The structure was exhibited at various key institutions amongst with University College London and during the International Association for Shell and Spatial Structures symposium (IASS) held in Amsterdam in 2015. A month solo exhibition took place in


August 2016 [52] at a well-known Building Technology gallery space called 'The Building Centre' situated in central London.

## Acknowledgments

The authors gratefully acknowledge the Engineering and Physical Sciences Research Council (EPSRC) who provided core funding for this project through UCL Doctoral Training Centre in Urban Sustainability and Resilience (Grant EP/G037698/1), as well as Expedition Engineering, the project industrial partner who provided significant additional resources. Building this prototype was also possible thanks to the contribution from the Institution of Civil Engineers Research and Development Enabling Fund and the Institution of Structural Engineers Research Award. Support from National Instruments in the form of training and technical assistance is gratefully acknowledged. EPFL Applied Computing and Mechanics Laboratory (IMAC) is thankfully acknowledged for their support during the review process of this article.

## ORCID iDs

Gennaro Senatore  <https://orcid.org/0000-0001-7418-9713>

Philippe Duffour  <https://orcid.org/0000-0003-3551-1217>

## References

- [1] Soong T and Chang J 1982 Active vibration control of large flexible structures *Shock Vib. Bull.* **52** 47–54
- [2] Soong T T 1988 State of the art review: active structural control in civil engineering *Eng. Struct.* **10** 74–84
- [3] Abdel-Rohman M and Leipholz H 1983 Active control of tall buildings *J. Struct. Eng.* **109** 628–45
- [4] Reinhorn A, Soong T, Riley M, Lin R, Aizawa S and Higashino M 1993 Full-scale implementation of active control. II: installation and performance *J. of Struct. Eng.* **119** 1935–60
- [5] Bani-Hani K and Ghaboussi J 1998 Nonlinear structural control using neural networks *J. Eng. Mech.* **124** 319–27
- [6] Rodellar J, Mañosa V and Monroy C 2002 An active tendon control scheme for cable-stayed bridges with model uncertainties and seismic excitation *Struct. Control Health Monit.* **9** 75–94
- [7] Xu B, Wu S and Yokoyama K 2003 Neural networks for decentralized control of cable-stayed bridge *J. Bridge Eng. (ASCE)* **8** 229–36
- [8] Schnellenbach M H and Steiner D 2013 Self-tuning closed-loop fuzzy logic control algorithm for adaptive prestressed structures *Struct. Eng. Int.* **24** 163–72
- [9] Preumont A, de Marneffe B, Deraemaeker A and Bossens B 2008 The damping of a truss structure with a piezoelectric transducer *Comput. Struct.* **86** 227–39
- [10] Henry A, Kam C, Smith M, Lewis C, King M, Boulter N, Hoad P, Wong R, Munro S and Ming S 2016 Singapore sports hub: engineering the National Stadium *Struct. Eng.* **94** 26–37
- [11] SCX, Wimbledon Centre Court Retractable Roof, 2010. <http://scxspecialprojects.co.uk/cache/filelibrary/73/library/fileLibrary/2011/6/Wimbledon.pdf> (Accessed: 15 09 2016)
- [12] Tibert G 2002 Deployable Tensegrity Structures for Space Applications *Doctoral dissertation* Royal Institute of Technology, Stockholm
- [13] Fest E, Shea K, Domer B and Smith F 2003 Adjustable tensegrity structures *J. Struct. Eng.* **129** 515–26
- [14] Adam B and Smith I F 2008 Active tensegrity: a control framework for an adaptive civil-engineering structure *Comput. Struct.* **86** 2215–23
- [15] Campanile L F 2005 Initial thoughts on weight penalty effects in shape-adaptable systems *J. Intell. Mater. Syst. Struct.* **16** 47–56
- [16] Hasse A and Campanile F 2009 Design of compliant mechanisms with selective compliance *Smart Mater. Struct.* **18** 115016
- [17] Jenkins C 2005 *Compliant Structures in Nature and Engineering* 1st edn (Southampton: WIT Press)
- [18] Weilandt A 2007 Adaptivität bei Flächentragwerken *Doctoral dissertation* University of Stuttgart, Stuttgart
- [19] Sobek W 1987 Auf pneumatisch gestützten Schalungen hergestellte Betonschalen *Doctoral dissertation* University of Stuttgart, Stuttgart
- [20] Neuhäuser S 2014 Untersuchungen zur Homogenisierung von Spannungsfeldern bei adaptiven Schalentragwerken mittels Auflagerverschiebung *Doctoral dissertation* University of Stuttgart, Stuttgart
- [21] Soong T and Cimellaro G 2009 Future directions in structural control *Struct. Control Health Monit.* **16** 7–16
- [22] Korkmaz S 2011 A review of active structural control: challenges for engineering informatics *Comput. Struct.* **89** 2113–32
- [23] Cha J, Pitarresi J and Soong T 1988 Optimal design procedures for active structures *J. Struct. Eng.* **114** 2710–23
- [24] Khot N 1998 Multicriteria optimization for design of structures with active control *J. Aerosp. Eng.* **11** 45–51
- [25] Lu L Y, Utku S and Wada B 1992 On the placement of active members in adaptive truss structures for vibration control *Smart Mater. Struct.* **1** 8–23
- [26] Begg D and Liu X 2000 On simultaneous optimization of smart structures: II. Algorithms and examples *Comput. Methods Appl. Mech. Eng.* **184** 25–37
- [27] Onoda J and Haftka R 1987 An approach to structure/control simultaneous optimization for large flexible spacecraft *AIAA J.* **25** 1133–8
- [28] Sobek W and Teuffel P 2001 Adaptive systems in architecture and structural engineering *Proc. SPIE* **4330** 36–45
- [29] Teuffel P 2004 Entwerfen Adaptiver Strukturen *Doctoral dissertation* University of Stuttgart, Stuttgart
- [30] Senatore G, Duffour P, Winslow P, Hanna S and Wise C 2013 Designing adaptive structures for whole life energy savings *Proc. 5th Int. Conf. on Structural Engineering, Mechanics and Computation (Cape Town)* (London: Taylor and Francis Group) pp 2105–10
- [31] Senatore G, Duffour P, Hanna S, Labbe F and Winslow P 2011 Adaptive structures for whole life energy savings *Int. Association for Shell and Spatial Structures (IASS)* **52** 233–40
- [32] British Standard 2005, BS EN 1993-1-8:2005 Design of Steel Structures
- [33] National Instruments, Strain Gauge Configuration Types, <http://ni.com/white-paper/4172/en/#toc10> (Accessed: 08 06 2015)
- [34] Industrifil, TAU cable, <http://industrifil.com/TAU36.html> (Accessed 06 2015)
- [35] Linak LA36, Linear Actuator LA36, <http://linak.co.uk/products/linear-actuators.aspx?product=LA36> (Accessed: 06 05 2016)
- [36] National Instruments NI Compact RIO, National Instruments, <http://ni.com/compactrio/> (Accessed: 06 05 2016)

- [37] Roboteq SDC2130, <http://roboteq.com/index.php/roboteq-products-and-services/brushed-dc-motor-controllers/sdc2130-detail> (Accessed: 06 05 2016)
- [38] Fylde Fylde Micro Analog 2, <http://fylde.com/microan2.htm> (Accessed: 06 05 2016)
- [39] TDK-Lambda AC to DC power supply-GWS, <http://uk.tdk-lambda.com/products/product-details.aspx?cid=1&scid=309> (Accessed: 06 05 2016)
- [40] Patnaik S, Hopkins D and Halford G 1991 Integrated force method versus displacement method for finite element analysis *Comput. Struct.* **38** 377–407
- [41] Reissner H 1931 Eigenspannungen und Eigenspannungsquellen *Z. Angew. Math. Mech.* **11** 1–8
- [42] Mura T 1991 *Micromechanics of Defects in Solids* 2nd edn (Dordrecht: Kluwer) (doi:10.1007/978-94-009-3489-4)
- [43] Irschik H and Ziegler F 2001 Eigenstrain without stress and static shape control of structures *AIAA J.* **39** 1985–90
- [44] DeWalt DW089K, <http://dewalt.co.uk/powertools/productdetails/catno/DW089K/> (Accessed: 06 2015)
- [45] Phidgets 3584\_0—CE-IZ04-35A2-1.0/0-50A DC Current Transducer, [http://phidgets.com/products.php?category=8&product\\_id=3584\\_0](http://phidgets.com/products.php?category=8&product_id=3584_0) (Accessed: 06 05 2016)
- [46] Shawe-Taylor J and Cristianini N 2004 *Kernel Methods for Pattern Analysis* (Cambridge: Cambridge University Press)
- [47] Senatore G Adaptive truss prototype demonstration <https://vimeo.com/gennarosenatore/adaptivetrussprototype>
- [48] Griffis L 1993 Serviceability limit states under wind load *Eng. J.* **30** 1–16
- [49] Patnaik S, Gendy A, Berke S and Hopkins D 1998 Modified fully utilized design (MFUD) method for stress and displacement constraints *Int. J. Numer. Methods Eng.* **41** 1171–94
- [50] Hammond G and Jones C 2008 Embodied energy and carbon in construction materials *Proc. Institution of Civil Engineers - Energy* **161** 87–98
- [51] LVDT LVDT, [http://meas-spec.com/product/t\\_product.aspx?id=2622](http://meas-spec.com/product/t_product.aspx?id=2622) (Accessed: 05 2015)
- [52] L. Building Centre Adaptive Structures Exhibition, 2016. <http://buildingcentre.co.uk/exhibitions/adaptive-structures> (Accessed: 11 2016)